Received: 29 May 2022 | Revised: 11 October 2022 | Accepted: 20 November 2022

IET Renewable Power Generation

DOI: 10.1049/rpg2.12649

The Institution of Engineering and Technology WILEY

ORIGINAL RESEARCH

Utilizing high fidelity data into engineering model calculations for accurate wind turbine performance and load assessments under design load cases

Galih Bangga[1,2] | **Steven Parkinson**[2] | **Thorsten Lutz**[1]

[1]University of Stuttgart, Institute of Aerodynamics and Gas Dynamics (IAG), Stuttgart, Germany

[2]DNV Services UK, One Linear Park, Bristol, United Kingdom

Correspondence
Galih Bangga, University of Stuttgart, Institute of Aerodynamics and Gas Dynamics (IAG), Pfaffenwaldring 21, 70569 Stuttgart, Germany.
Email: galih.bangga@dnv.com

Abstract

Wind turbines often have lower performance and experience higher loading in real operation compared to the original design performance. The reasons stem from the influences of complex atmospheric turbulence, blade contamination, surface imperfection and airfoil-shape changes. Engineering models used for designing wind turbines are limited to information derived from blade sectional datasets, while details on the three-dimensional blade characteristics are not captured. In these studies, a dedicated strategy to improve the prediction accuracy of engineering model calculations will be presented. The main aim is to present an elaborated effort to obtain a better estimate of the turbine loads in realistic operating conditions. The present studies are carried out by carefully utilizing data from high fidelity Computational Fluid Dynamics (CFD) computations into Blade Element Momentum (BEM) and Vortexline methods. The results are in a good agreement with detailed field measurement data of a 2.3 MW turbine. The studies are further extended to a large turbine having a rated power of 10 MW to provide an overview of its suitability for large turbines. Finally, calculations of the wind turbine under a realistic IEC design load case are demonstrated. The studies highlight important considerations for engineering modeling using BEM and Vortexline methods.

1 | INTRODUCTION

The aerodynamics of a wind turbine rotor is highly complex and it has become the subject of interest for many decades. Understanding the physics of this phenomenon is of importance to enable an accurate estimation of the wind turbine loads, having a direct implication to an improved wind turbine design strategy. The complexity results from interactions between the inflow conditions such as wind shear, yaw and turbulence with the highly three-dimensional flow on the rotor blade, and this provides a direct challenge to the rotor design [1].

Various modeling strategies have been developed throughout the years. These include the simplest of hands calculations to sophisticated numerical approaches. Among the modeling approaches, the Blade Element Momentum (BEM) theory is considered as the state-of-the-art method in wind turbine design especially in industry. This method is relatively simple, fast, robust and reliable in most flow situations within its limit. The works of Betz [2] and Glauert [3–5] are believed to be the basic foundation of all various available BEM methods. Principally, BEM models the rotor as a rotating permeable disk which extracts the energy from the flow. As a consequence, forces are generated and depending on the modeling strategies, these forces can be applied on the rotor area or at the local blade segment. BEM usually relies on the defined sectional aerodynamic characteristics which can be obtained from the polar data in forms of the tabulated lift (C_L), drag (C_D) and moment (C_M) coefficients.

Since BEM is inherently a pure low-dimensional approach, it comes with many assumptions [1, 4–12] which are not always valid in all conditions. One of the example is the missing three-dimensional effects in BEM modeling. These effects are prominent in the area where the local flow gradients are large, especially in the near blade tip and root areas. Despite that, the physical mechanisms of the three-dimensional effects at

these two distinct locations are inherently different. The effect near the tip area is mainly caused by the assumption of the infinite blade number in BEM, while in fact the number of blades is limited. This causes flow field discrepancy and the angle of attack seen by the blade section is altered. As a consequence, the access to the look up table of the polar data in the near tip area needs to be adjusted to account for this effect. Several tip loss models are available and can be used to correct the loads acting at this region, for example, by using the Prandtl tip loss model [13] or Shen model [14]. As an alternative to BEM, the higher fidelity Vortexline method is proven beneficial for modeling the tip loss effect. The solutions of the Vortexline method is based mainly on the induction calculations employing the Biot-Savaart law. The method does not require any empirical correction model near the tip because the three-dimensional interactions are considered in the analyses.

The effect in the root area is more complex because it involves nonlinear interactions of the separated flow at high angle of attack and three-dimensionality of the flow itself. This difficulty remains true both for BEM and Vortexline based computations. Himmelskamp [15] was the first to discover the characteristics by evaluating the sectional aerodynamic forces of a rotating propeller and comparing the data with two-dimensional measurements. Under the influence of this effect (also commonly referred as the rotational augmentation), the sectional lift coefficient in the blade root is significantly higher than the two-dimensional (2D) conditions [16]. Traditionally, this effect is thought to be relevant only for old turbines having stall controlled mechanisms. Bangga et al. [16, 17] demonstrated that the effect is still very strong for large wind turbines because flow separation is even more pronounced for the employed thick airfoils. Empirical correction models such as those from Lindenburg [18], Bak et al. [19], Chaviaropoulos and Hansen [20] or Du & Selig [21] may be applied to model the rotational augmentation effect in the blade root area. Despite that, these correction models were developed long time ago for small wind turbine sizes. Calibration of the constants is rarely documented when the turbine size changes over the time. Empirical correction models often fail to deliver good prediction accuracy under such condition due to the complexity of the flow physics. Furthermore, there is no guarantee that the model works as expected for challenging flow conditions.

This three-dimensional effect becomes more difficult to predict when the turbine is operating under strong unsteadiness due to dynamic stall or atmospheric turbulence. Computational Fluid Dynamics (CFD) approaches offer an improved accuracy in modeling the three-dimensional flow in the root area of wind turbine blades [16]. The method has been proven to be reliable even under complex flow conditions in numerous studies [16, 22–27]. Despite that, it is well known that CFD is not suitable for computing all load cases due to its high computational cost. A question then arrives if one will be able to utilize partial data from CFD simulations and to incorporate the results into engineering model computations to improve their accuracy for various design load cases.

A proposal was made to replace the polar data of engineering model calculations with the polar data obtained from CFD simulations [1, 28]. This was done to incorporate partial inclusion of the three-dimensional effect into engineering model based simulations. Bangga [28] demonstrated that the polar data extracted from 3D CFD simulations was able to be adopted into BEM calculations, and the computed loads using BEM matched the loads obtained from CFD computations. A similar study was done by Schneider et al. [29] who evaluated different angle of attack extraction methods and by Guma et al. [30] for a relatively small wind turbine size. However, all these studies [28–30] were limited to steady flow conditions that match the situation in which the polar data was generated from. Further elaboration was done by Bangga and Lutz [1] who took the influence of the turbulent flow into account. Thy demonstrated that the proposal can be adopted for cases involving turbulent flows. However, this study was only limited to medium size wind turbine. Further studies are required to investigate the suitability of the 3D CFD polar for large wind turbines in complex conditions. Moreover, a consideration of the realistic inflow situation according to IEC (international electrotechnical commission) is required to assess the effects of the polar data against standardized turbine design conditions. The present paper is aimed at investigating the feasibility of incorporating the 3D CFD data into engineering model computations for wind turbines with different rotor sizes. Various flow conditions will be considered to enable comprehensive evaluations and to be able to verify the suitability of the approach. The results will be compared against high fidelity CFD computations and experimental data. Discussions will be provided in detail in terms of the resulting loads and the associated physical effects. The studies shall provide suggestions in the usage of the high fidelity data into engineering model simulations and will highlight possible improvements in future engineering model developments.

The present paper is structured as follows. Section 2 presents the investigated turbine, calculation methods and the process chain of the simulation strategy. The results are discussed in Section 3 and conclusion is given in Section 4.

2 | RESEARCH METHODOLOGY

2.1 | Studied wind turbine

2.1.1 | The 2.3 MW NM-80 turbine

The 2.3 MW NM-80 wind turbine measured within the framework of the DanAero project [31] was chosen as the first investigated turbine in the present studies. Detailed field measurement data is available for this turbine blade and accessible through a mutual collaborative work within the IEA Wind Task 29 project (now Task 47) [32]. During the DanAero measurement campaign, a number of innovative and coordinated

FIGURE 1 DanAero measurement site and the position of the turbine as well as the meteorology mast [31]

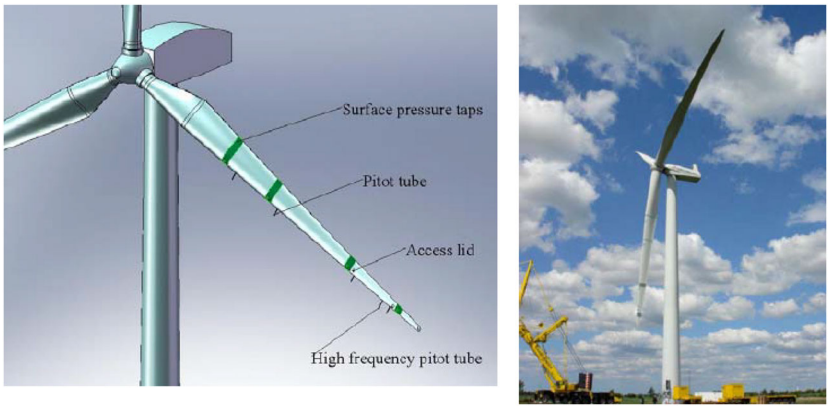

FIGURE 2 Illustration of the DanAero turbine and the installed machine on the site [31]

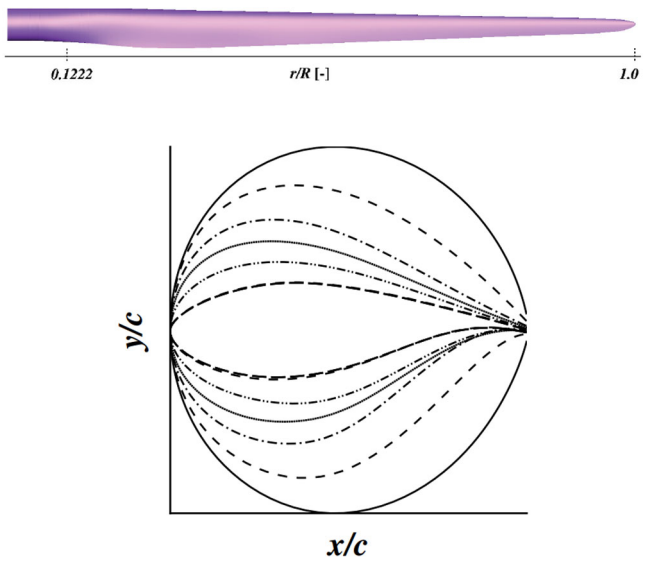

FIGURE 3 Illustration of the AVATAR wind turbine blade and its local airfoil sections having a rotor radius of 102.9 m [16]

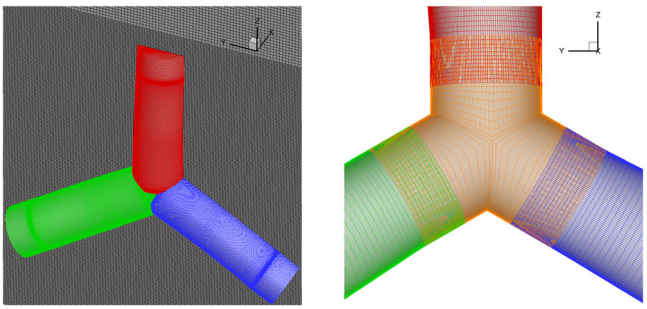

FIGURE 4 Illustration of the Chimera mesh topology for simulating wind turbines in FLOWer

measurements on two full scale MW turbines as well as wind tunnel measurements on various airfoil sections were carried out. The project was aimed at investigating the relationships between atmospheric and wake turbulence on turbine performance, loading and stability. The measurement was located in a small wind farm at Tjaereborg as depicted in Figure 1. In the

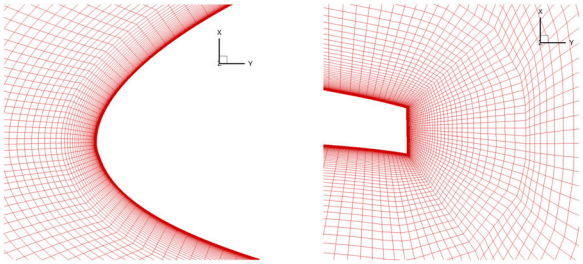

FIGURE 5 Overview of the blade mesh near the leading edge and trailing edge areas

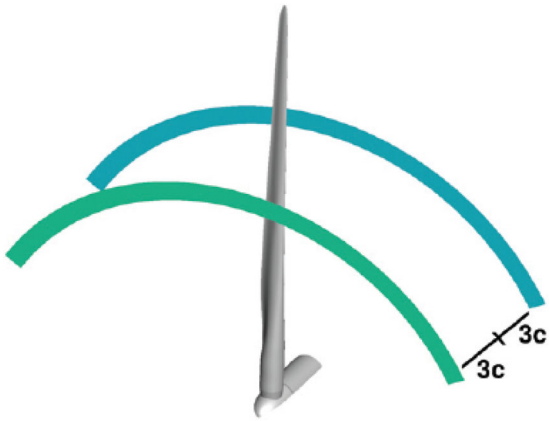

FIGURE 6 Illustration of the monitoring positions for extracting the sectional polar characteristics [16]

field measurement campaign, the aerodynamic loads in chord normal and tangential directions at four blade stations were recorded. These blade sectional loads were obtained by integrating the pressure distributions which were measured during the campaign. The locations of the pressure sensors and the illustration of the blade shape are given in Figure 2. The studied NM-80 turbine has a rotor diameter of 80 m, a tilt angle of 5° and a prebend of 1.4 m at the blade tip.

2.1.2 | The 10 MW AVATAR turbine

The second turbine chosen for the investigation was the 10 MW AVATAR turbine [33]. This turbine was designed based on the DTU 10 MW reference wind turbine [34] by enlarging the rotor size but keeping the rated power. A scaling factor of around 1.15 was applied. This directly yields in the smaller rated wind speed for the AVATAR turbine. This also implies that the turbine is operating at a smaller induction factor, reduced to below 1/3, resulting in $0.23 < a < 0.28$ to capture more power from lower wind speeds but reducing the loads. This design concept is denoted as low induction rotor (LIR) concept. This results in a slender blade design as illustrated in Figure 3. The AVATAR turbine has a diameter as large as 205.8 m (a radius of 102.9 m). The blade of the AVATAR turbine was tapered and twisted to obtain appropriate aerodynamic loading.

2.2 | Code description

2.2.1 | FLOWer

The FLOWer code was adopted as the main workforce for performing CFD simulations in the present studies. The code was originally developed by the German Aerospace Center (DLR) [35], but has undergone significant improvement in helicopter and wind turbine simulation capabilities in the last decade at the University of Stuttgart [36–39]. FLOWer is a compressible code and solves the three-dimensional Navier-Stokes equations in an integral form with several turbulence models available. For the present studies, the Menter Shear Stress Transport (SST) model [40] was chosen as this model was proven to be accurate for flow with relatively large pressure gradient. For complex flow involving atmospheric turbulence, this turbulence model was coupled to a large eddy simulation (LES) approach through the usage of the hybrid high fidelity RANS/LES modeling. The delayed-detached eddy simulation (DDES) was chosen for this modeling strategy for an improved treatment of the gray area problem and to avoid the occurrence of grid induced separation.

Block-structured grids were used to discretize the physical problem into the numerical domain. The spatial discretization applied a second order central discretisation with an artificial damping according to Jameson-Schmidt-Turkel (JST) [41] to obtain a second order or accuracy on smooth meshes. For simulating inflow turbulence and for properly resolving the wind turbine wake, the 5th order weighted essentially non-oscillatory scheme (WENO) [42] was used in the surrounding area outside the boundary layer domain. Time integration was done by an explicit multi-stage scheme adopting the dual time stepping method as implicit scheme. The turbulence model equations were solved separately from the main flow equations using a full implicit time integration method. The Message-Passing Interface (MPI) approach was adopted for the parallel computations.

FLOWer adopts an overlapping (Chimera) grid strategy for modeling wind turbine components. This mesh strategy simplifies the grid generation because it can be done separately for each turbine component while retaining the quality of the mesh. Figures 4 and 5 illustrate the Chimera mesh strategy applied for the 2.3 MW NM-80 turbine in the present studies.

For all simulations in the present paper, the boundary layer was fully resolved. This means that the height of the first cell layer was kept below $y^+ < 1$. For the rotor blade, the average y^+ level is 0.778. This is necessary to resolve the laminar sub-layer near the wall for the turbulent flow and since no wall function was employed. The growth rate in the boundary layer regime was kept 1.1. The blade mesh is one of the most important part in wind turbine analyses using CFD. For this paper, a mesh of 9 million cells was applied to model the blade of the 2.3 MW turbine blade and a mesh of 11 million cells was applied on the 10 MW turbine blade. Blade mesh convergence studies have been done in advance to ensure the solutions are independent of the mesh number [1, 17]. Depending on the type of the simulations, the resolution of the other mesh components (e.g. background

TABLE 1 Test cases considered for extracting the 3D CFD polar data

Turbine	U_∞ [m/s]	n [rpm]	α_p [deg]	α_s [-]	φ [deg]	TI_X [%]	TI_Y [%]	TI_Z [%]	Models
2.3 MW NM-80	3–25	12.3	−0.15	0	0	0	0	0	CFD
10 MW AVATAR	3–25	9.02	0	0	0	0	0	0	CFD

mesh) was adjusted. For example, the total number of mesh is about 27 million cells for generating the steady state solutions required for the polar data extraction (see Section 2.3). This was done by modeling only one blade by applying a periodic boundary condition. On the other hand, the simulations involving inflow turbulence and considering wake interaction amount cells number of higher than 100 million. Transient CFD solutions need to be obtained for this large cells number for every single time step size of around 2 degrees of blade rotation per physical step.

2.2.2 | Bladed

Bladed is an engineering tool used in numerous wind turbine industries and in research environment. The code long history dates back to early 1990s at the consulting office at the university by Dr. Andrew Garrad and Dr. Unsal Hassan to date being one of the major software for wind turbine design at DNV. Commercially the code uses the solutions of the BEM equations to obtain the aerodynamic loads experienced by the wind turbine. The code has been improved over the time accommodating several latest development in the field, for example, better handling of the polar gradient for dynamic stall modeling, the inclusion of the structural velocity in induction calculations, improved calculation speed and integrated wind turbine aero-structural offshore platform analyses. Several publications documented verification studies of the Bladed code performance [32, 43–50].

The engineering modeling in Bladed aerodynamics is based on classical BEM theory where the axial and tangential Glauert momentum equations are expressed in dimensional form instead of non-dimensional factors. The dynamic submodels such as the skew wake correction are represented in a full state space forms which allow a direct integration of the aerodynamic and structural states. These were made possible via the Generalized-α integrator [51]. For the present studies, the time step size for the fixed step integration was set to 0.02 s. The tip loss effect was modeled by employing the Prandtl tip loss correction [13]. This modifies the induction by providing a "fade out" function which scales the level of the mass flow along the blade radius. Furthermore, Bladed solutions were also coupled with the high induction correction according to Glauert [3–5] and with the state-of-the art Beddoes-Leishman dynamic stall model [52]. The incompressible forms [53] of the equations were adopted in these studies incorporating the impulsive lift and pitching moment contributions.

Next to the classical BEM model, a fully coupled free wake lifting line (Vortexline) model can be used in Bladed. This model is currently available for internal purpose only and not yet commercially released into the market. The basic theory of the implementation strategy was described by Kloosterman [54]. The following works documented the performance of the Bladed Vortexline model [45, 46, 55, 56]. The code is run in parallel and adopts vectorized implementation to accelerate the running time. The Vortexline model in Bladed has been recently improved for better convergence treatment and capabilities in calculating the loads at the blade sections.

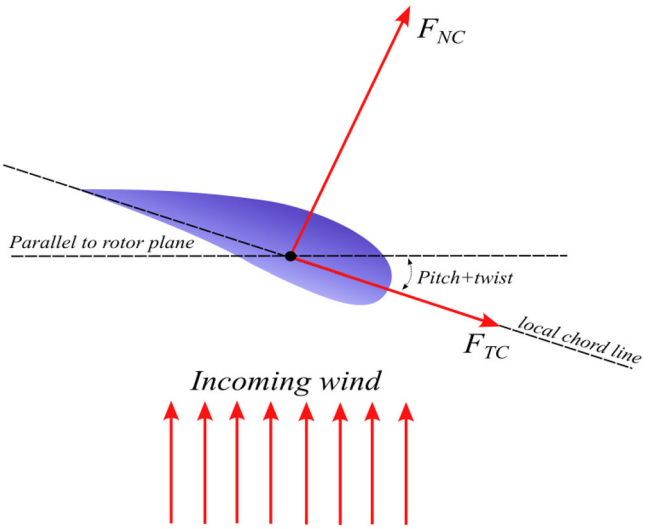

FIGURE 7 Definition of the sectional forces at the blade element used for the evaluations. F_{Nc} represents the normal force, perpendicular to the local chord line; F_{Tc} represents the tangential (chordwise) force, parallel to the local chord line

2.3 | Extraction of the 3D CFD polar data

In this paper, the data from the high fidelity CFD simulations will be adopted into engineering model simulations for an improved accuracy. It is agreed that engineering models like BEM and Vortexline rely heavily upon the polar data. Therefore, providing reliable polar datasets will be the key for achieving accurate computations. The proposal for replacing the standard polar data, two-dimensional data corrected using empirical models, with the higher fidelity 3D CFD data will be adopted in the present studies. Despite that, it is not a trivial matter to perform such a task because the flow field of a rotating wind turbine blade is not directly accessible in the simulations. The effective angle of attack is a key parameter that needs to be considered, which is influenced by the effects of bound circulation

TABLE 2 Test cases considered for the 2.3 MW wind turbine computations

Case	U_∞ [m/s]	n [rpm]	α_p [deg]	α_s [-]	φ [deg]	TI_X [%]	TI_Y [%]	TI_Z [%]	Models
Case A.1	9.792	16.2	−4.75	0.249	−6.02	0	0	0	CFD/BEM/Vortexline
Case A.2	9.792	16.2	−4.75	0.249	−6.02	5.16	3.612	2.58	CFD/BEM/Vortexline

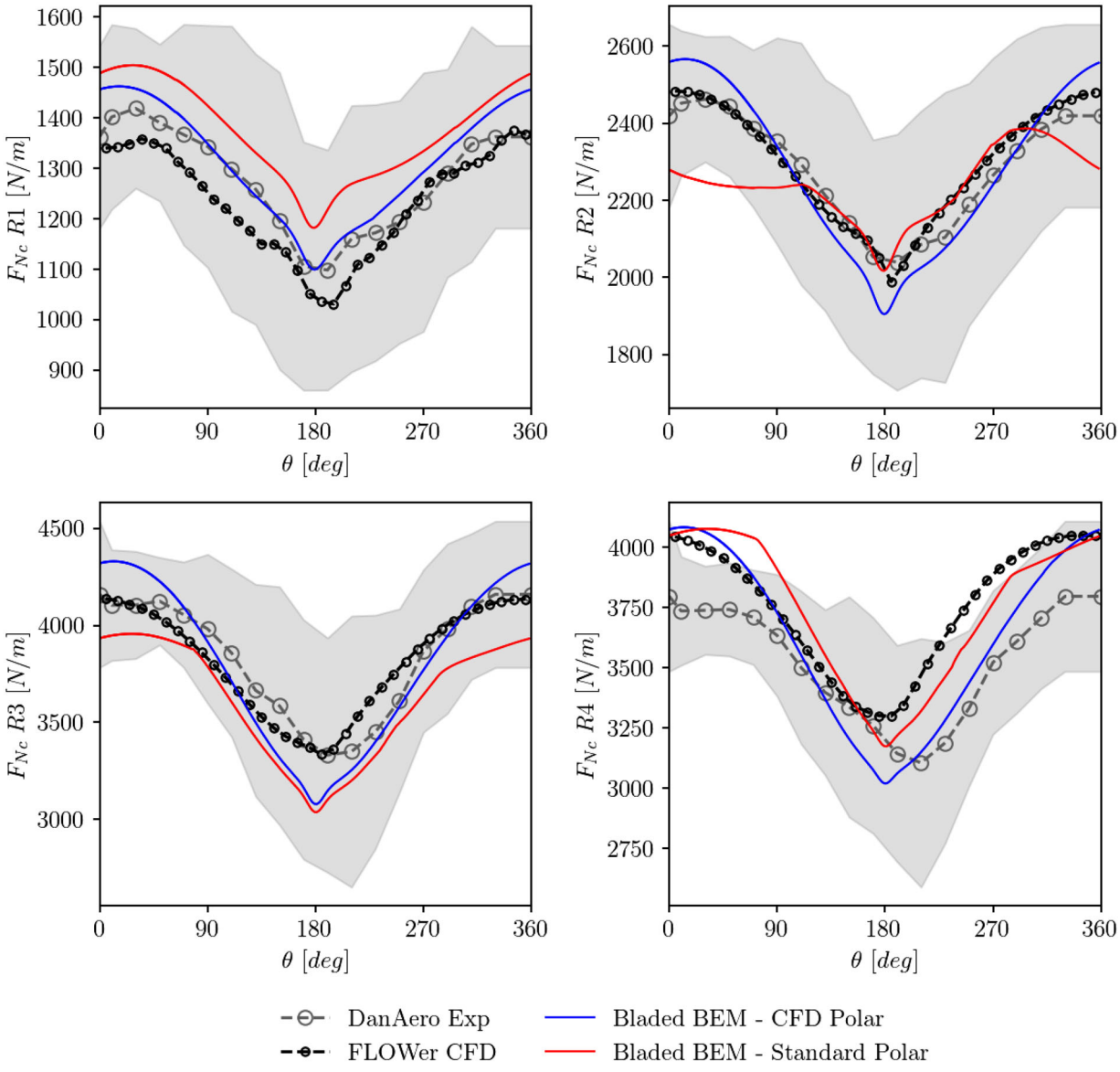

FIGURE 8 Azimuthal normal force comparison between BEM, CFD and measurement data for Case A.1. Four radial stations are reported: $R1 = 13$ m ($0.325R$), $R2 = 19$ m ($0.475R$), $R3 = 30$ m ($0.75R$), $R4 = 37$ m ($0.925R$)

and wake, including the shed- and trailing-vortices and inductions. Thus, it cannot be obtained directly from the blade surface pressure data.

The reduced axial velocity technique, also known as the azimuthal averaging technique, according to Hansen et al. [57] was used to extract the angle of attack and to obtain the sectional polar data. As briefly mentioned in Section 2.2.1, only one blade was modeled in this extraction by adopting flow periodicity. Steady state solutions were aimed and thus it accelerated the computational time significantly compared to the transient simulations in complex flow conditions. During the simulation, the velocity was monitored at two axial locations upstream and downstream of the rotor plane, covering an azimuth angles of −60° to +60°, see Figure 6. The velocity components at the

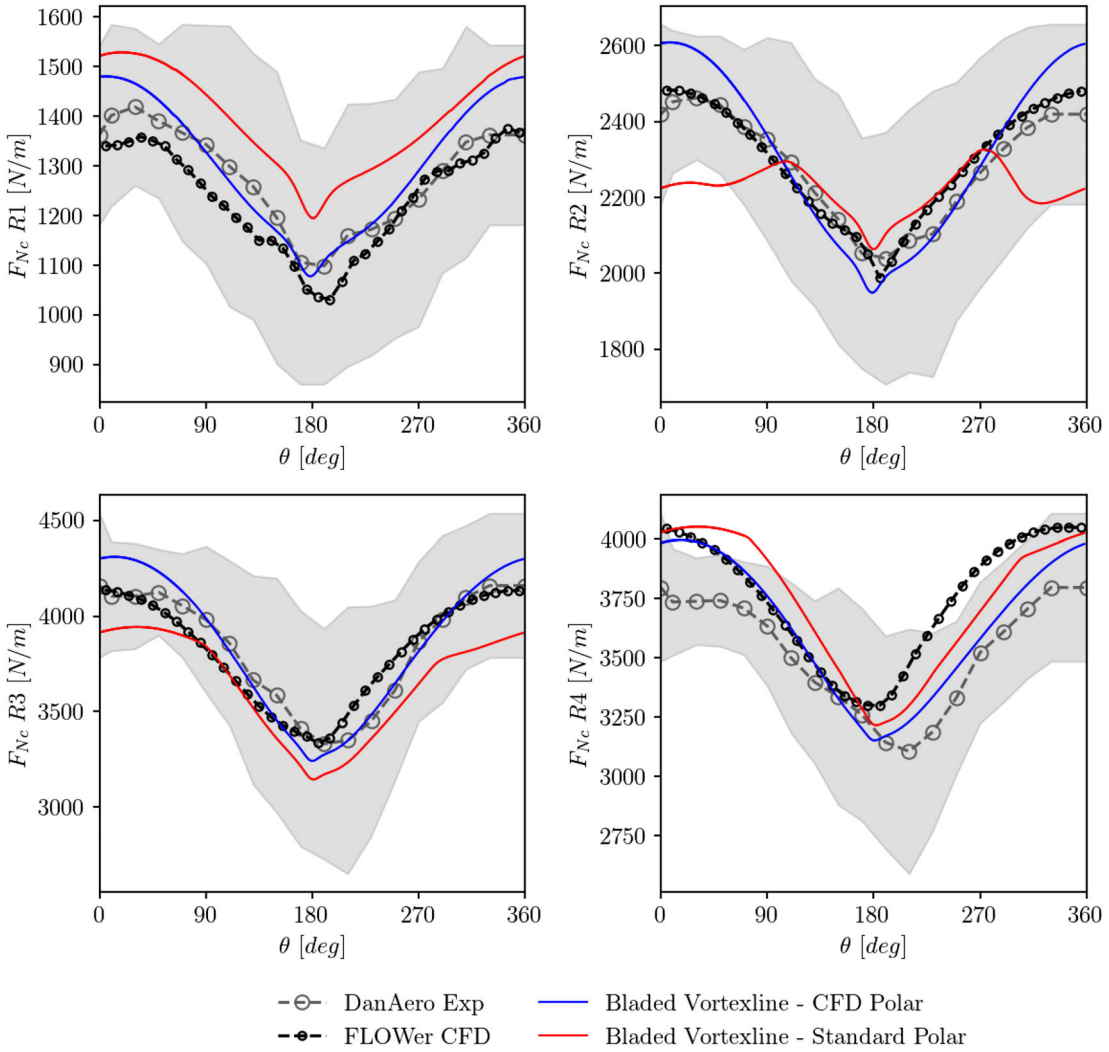

FIGURE 9 Azimuthal normal force comparison between Vortexline, CFD and measurement data for Case A.1. Four radial stations are reported: $R1 = 13$ m ($0.325R$), $R2 = 19$ m ($0.475R$), $R3 = 30$ m ($0.75R$), $R4 = 37$ m ($0.925R$)

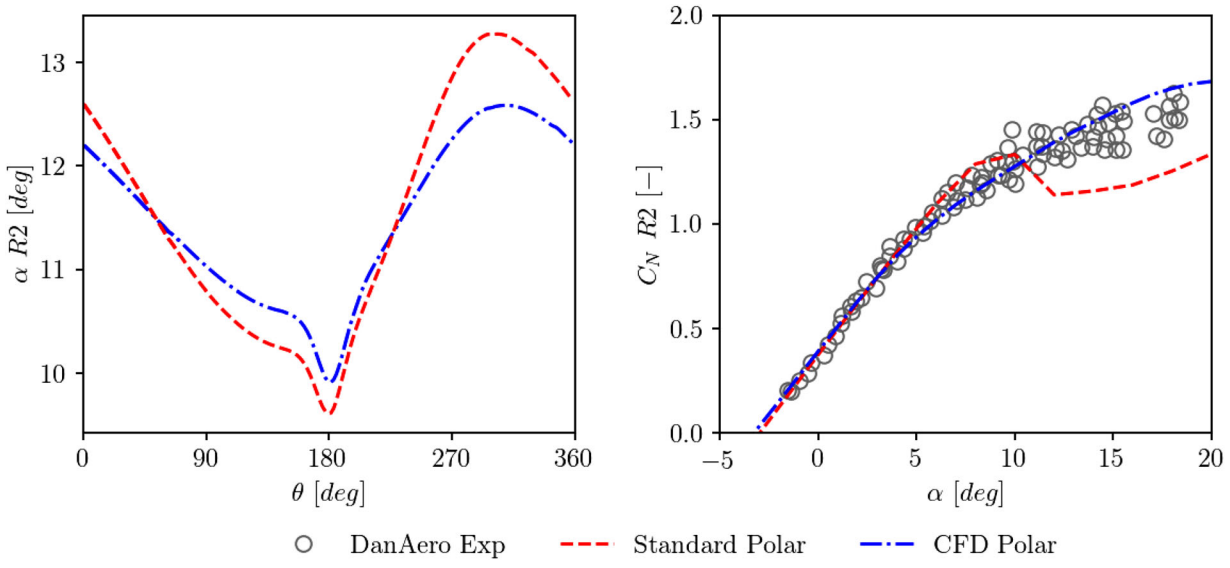

FIGURE 10 Angle of attack variation from Vortexline simulations and the associated input polar data in comparison with field measurement. The polar data (in forms of C_L and C_D) are transformed to chord normal direction (C_N) to conform with the measured values. Direction of the C_N is inline with F_{Nc} in Figure 7

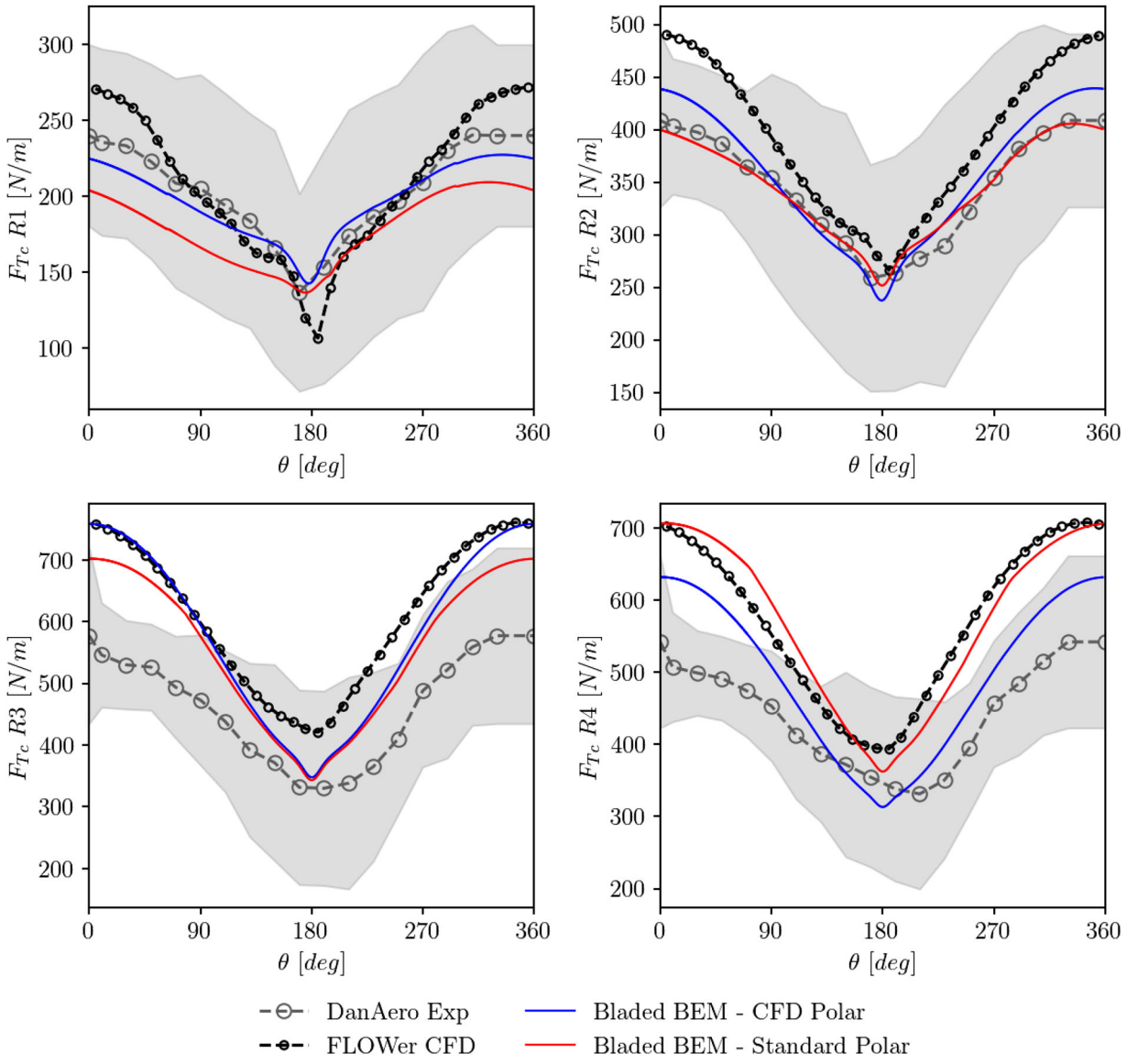

FIGURE 11 Azimuthal chordwise force comparison between BEM, CFD and measurement data for Case A.1. Four radial stations are reported: $R1 = 13$ m ($0.325R$), $R2 = 19$ m ($0.475R$), $R3 = 30$ m ($0.75R$), $R4 = 37$ m ($0.925R$)

rotor plane were obtained by averaging the velocity components from these two monitoring positions, then the sectional polar characteristics could be derived. To obtain the full set of the polar data, simulations were performed by varying the incoming wind speed at a constant rotational speed and a constant pitch angle. For the present studies, the setup listed in Table 1 was used for the polar data extraction process by means of the CFD simulations.

The extracted polar data includes all the three-dimensional effects along the blade radius. For Vortexline simulations, the three-dimensional effect in the near tip area should be removed because it is included already in the basic of Vortexline calculations. There is no "switch" to turn the tip loss effect off for the Vortexline based calculations. This is necessary to avoid having the tip effect applied twice. To do so, the 3D polar data was applied only for the first 90% of the blade stations. The remaining 10% was obtained from 2D CFD simulation of the local blade section considering the Reynolds number at the rated turbine operation. The combined 3D-2D CFD polar data can be denoted as the "hybrid polar".

2.4 | Inflow generation

The turbulent inflow was generated differently for CFD and engineering model simulations. This is due to the fact that CFD and engineering models have different assumptions in reading the inflow data, for instance the assumption of frozen turbulence or the Taylor's hypothesis in engineering modeling.

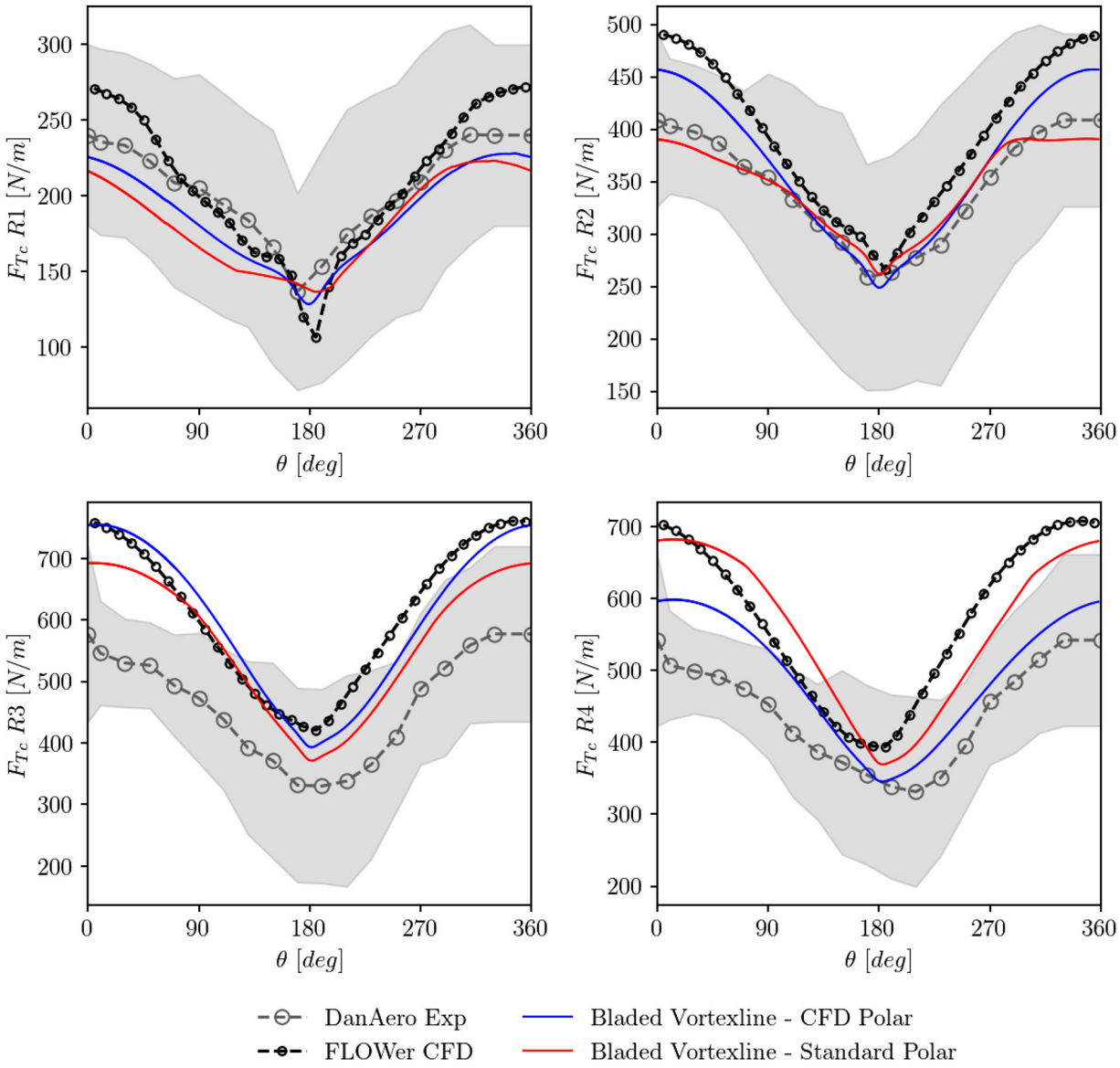

FIGURE 12 Azimuthal chordwise force comparison between Vortexline, CFD and measurement data for Case A.1. Four radial stations are reported: $R1 = 13$ m ($0.325R$), $R2 = 19$ m ($0.475R$), $R3 = 30$ m ($0.75R$), $R4 = 37$ m ($0.925R$)

To impose the inflow turbulence in CFD, velocity fluctuations (u') in three directions in space were injected at a desired position upstream of the rotor plane using a momentum source term [58]:

$$f_{Ei} = \frac{\rho u_i'}{\Delta x_n}\left(U_n + \frac{1}{2}u_n'\right), \tag{1}$$

where the subscript n represents the normal component to the turbulence plane. The turbulent fluctuations were superimposed with the mean wind speed. This approach allows one to apply turbulence closer to the rotor plane, minimizing the effect of numerical dissipation when turbulence is propagated.

Specifically for a direct comparison of the timeseries alignment between engineering models and CFD, the turbulent inflow needs to be prepared in a specific manner. If this is the intention, the artificially generated inflow turbulence (e.g. using Kaimal or Mann models) cannot be directly used in engineering model (unless only statistics or mean values will be compared). This is due to the fact that turbulence is applied directly on the rotor plane for engineering model while it is at a specified distance upstream of the rotor for CFD. Furthermore, turbulence is frozen in engineering models. In contrast, turbulence propagation is slowing down approaching the rotor in CFD since the energy of the flow is extracted by the rotor. To account for these effects, the turbulent inflow can be generated by extracting the flow field from CFD simulations without rotor (Empty Box simulation). The time shift can be calculated by quantifying the timeseries correlation of the Empty Box data with an equal simulation but with the rotor being present. The time shift is

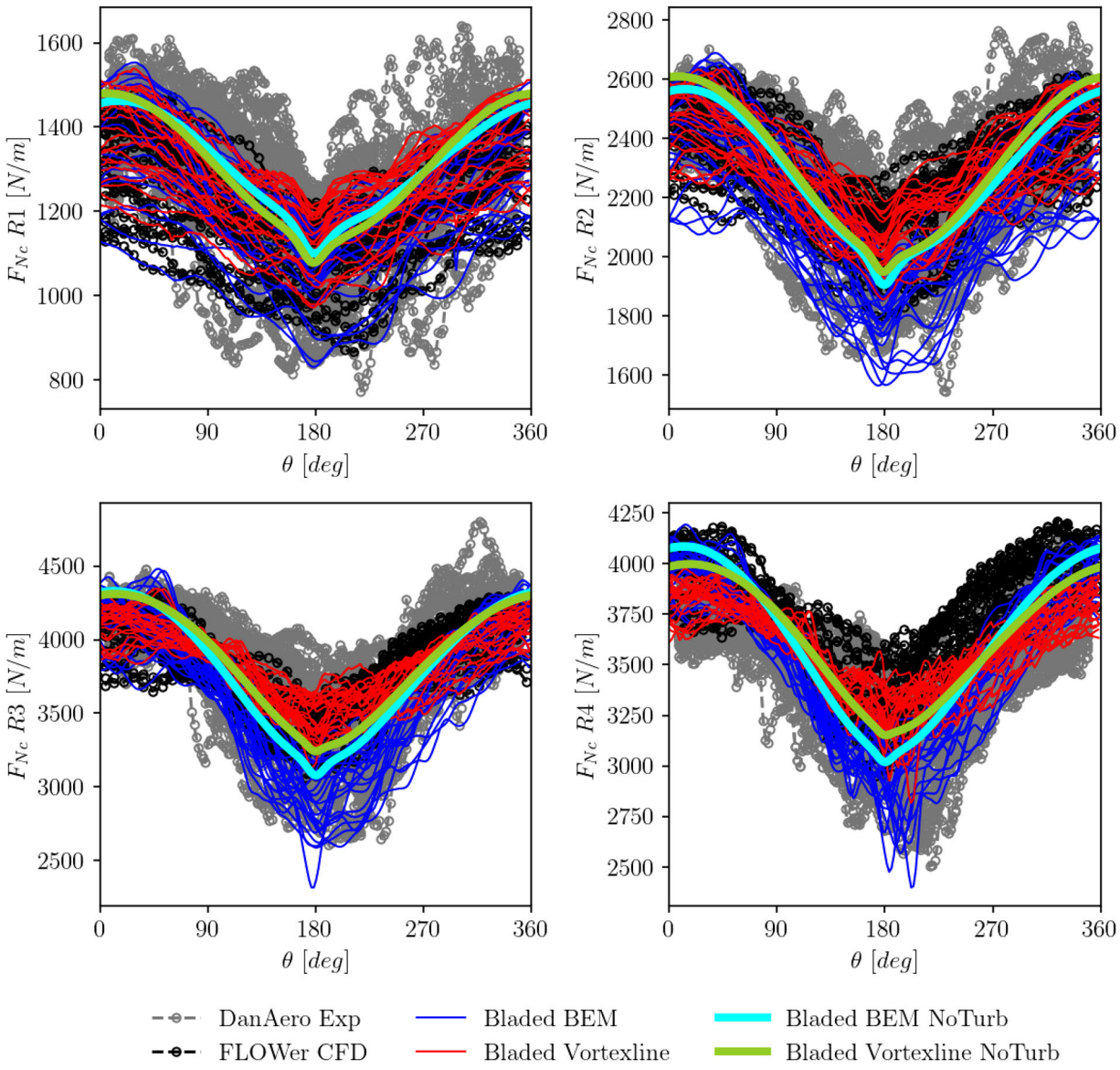

FIGURE 13 Azimuthal normal force comparison between BEM, Vortexline, CFD and measurement data for Cases A.1 and A.2. Four radial stations are reported: $R1 = 13$ m ($0.325R$), $R2 = 19$ m ($0.475R$), $R3 = 30$ m ($0.75R$), $R4 = 37$ m ($0.925R$)

searched by varying τ in the following formulation:

$$C_{ii}(x, y, z, \tau) = \frac{\sum_{t=t_0}^{T} \left[u'_{i,Empty}(x, y, z, t+\tau) \cdot u'_{i,Rotor}(x, y, z, t) \right]}{\sqrt{\sum_{t=t_0}^{T} \left[\left(u'_{i,Empty}(x, y, z, t+\tau) \right)^2 \cdot \left(u'_{i,Rotor}(x, y, z, t) \right)^2 \right]}}, \tag{2}$$

where the optimal alignment is obtained by maximizing $C_{ii}(x, y, z, \tau)$. The usage of this approach has been documented and verified in [1, 59]. This method was applied on cases where CFD data is available for comparing the timeseries in Sections 3.1 and 3.2. For modeling the flow data in Section 3.4, the standard Kaimal turbulence generator was adopted instead.

3 | RESULTS AND DISCUSSION

The results of the present studies will be presented and discussed in this section. The analyses are divided into three different categories: for the 2.3 MW turbine in Section 3.1, for the 10 MW turbine in Section 3.2 and the simulations considering an IEC design load case in Section 3.4. The investigations performed in this paper are focused at the detailed local characteristics of the blade sections. Figure 7 illustrates the adopted definition of the sectional forces at the blade element.

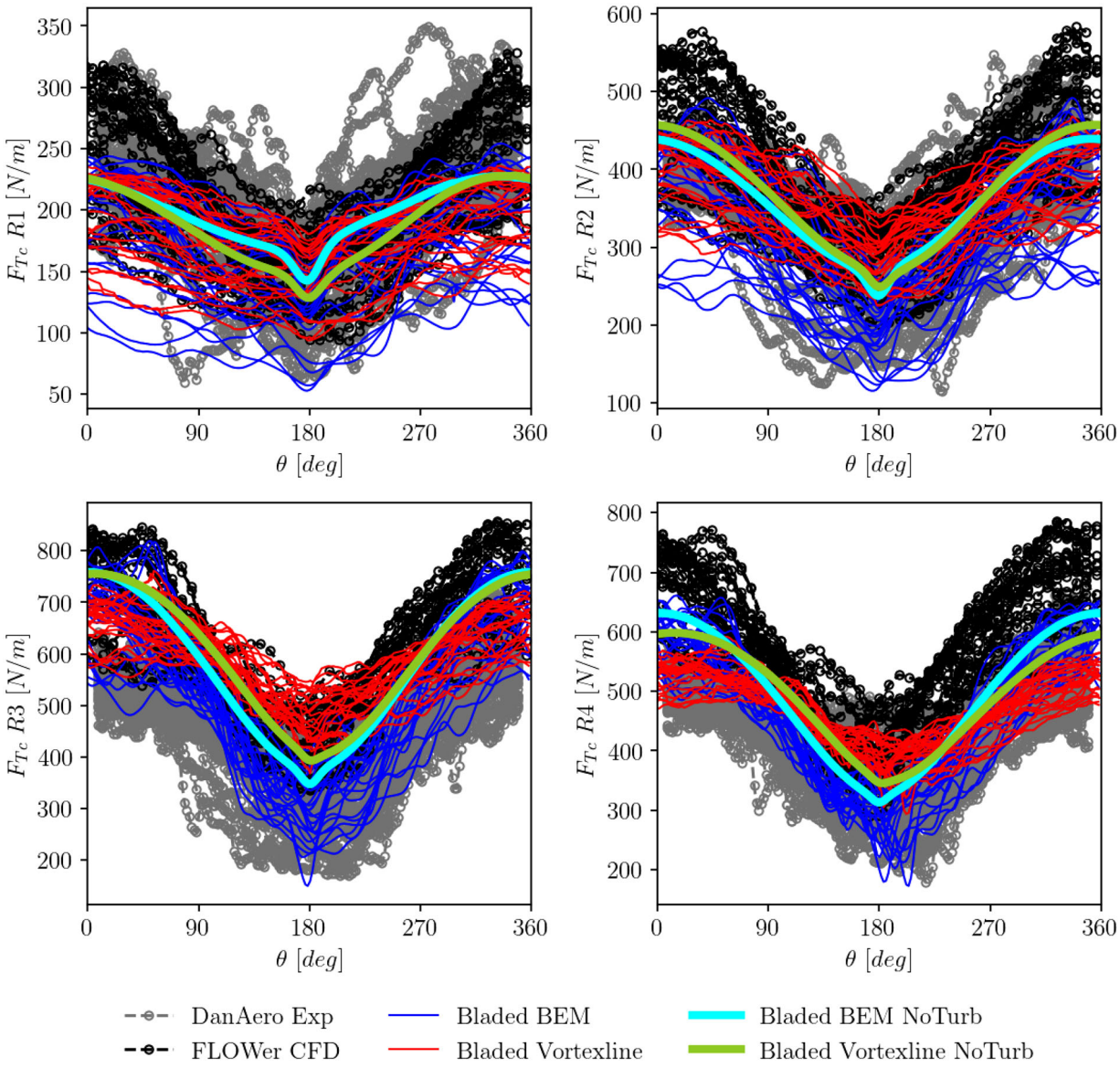

FIGURE 14 Azimuthal chordwise force comparison between BEM, Vortexline, CFD and measurement data for Cases A.1 and A.2. Four radial stations are reported: $R1 = 13$ m ($0.325R$), $R2 = 19$ m ($0.475R$), $R3 = 30$ m ($0.75R$), $R4 = 37$ m ($0.925R$)

3.1 | 2.3 MW wind turbine

Two different test cases were considered for this turbine as listed in Table 2. Both tests have effectively the same turbine setup and most flow conditions. They are exposed to a wind speed $U_\infty = 9.792$ m/s, a rotational speed (n) of 16.2 rpm, a wind shear exponent (α_s) of 0.249, at a constant pitch angle (α_p) of $-4.75°$ and under a constant mean yaw misalignment (φ) of $-6.02°$. The main distinction between the two test cases lies in the inclusion of the inflow turbulence with in all directions for Case A.2, whereas the flow is inherently steady for Case A.1. This inflow turbulence was generated based on the process described in Section 2.4.

3.1.1 | The effects of polar data

This section highlights the importance of polar data for obtaining accurate engineering model calculations. Two polar datasets were considered. The first polar data is the "standard polar" which was based on wind tunnel measurement of 4 airfoils constructing the blade. This polar data was corrected to account for the 3D effects using an empirical model according to Bak et al. [19]. In contrast to the standard polar model, data from the high fidelity CFD results was extracted and the sets of the resulting aerodynamic polar were applied on the second model "CFD polar". The extraction process is described in Section 2.3. Furthermore, a fully resolved CFD simulation was

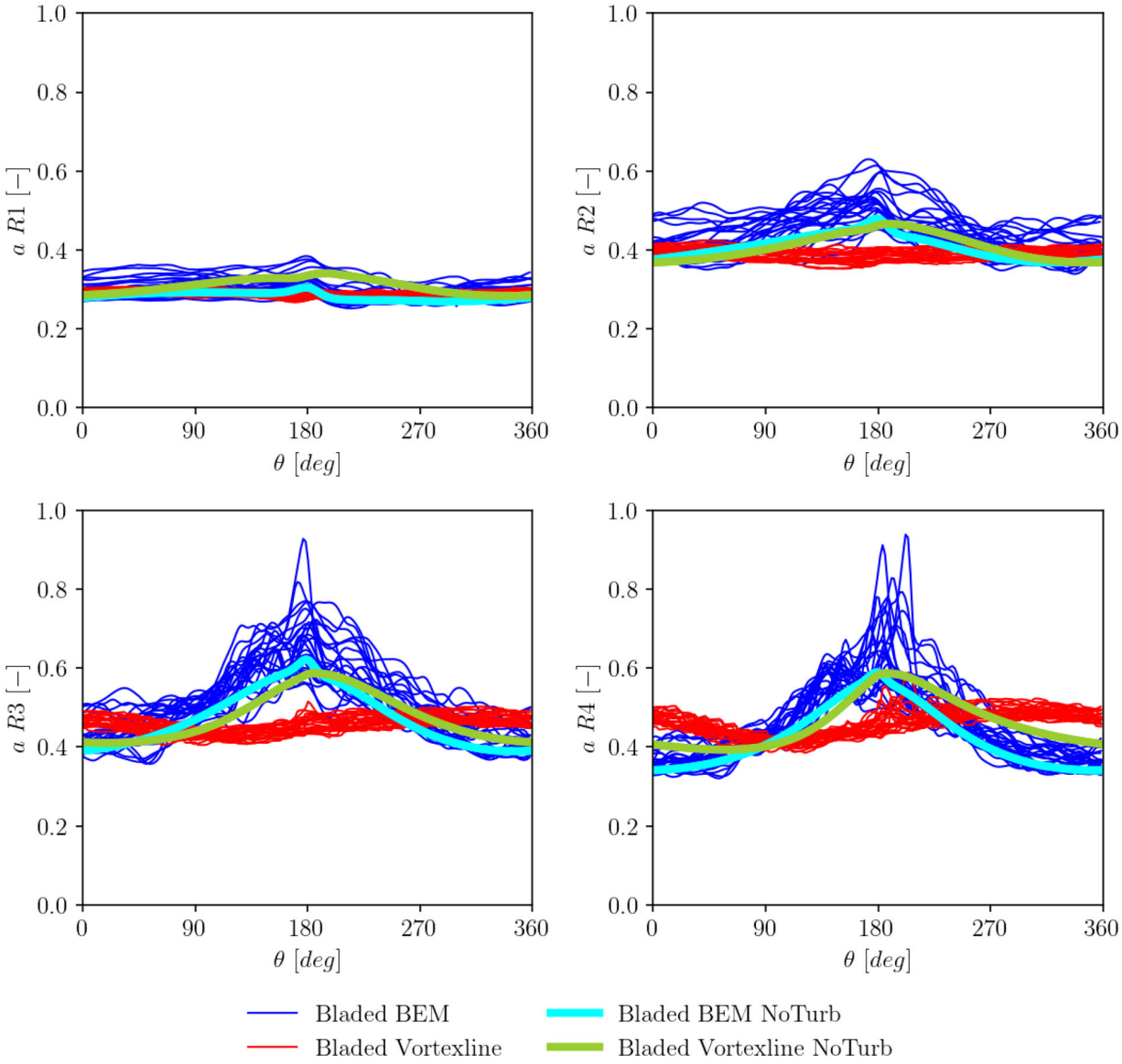

FIGURE 15 Induction dynamics comparison between BEM and Vortexline results for Cases A.1 and A.2. Four radial stations are reported: $R1 = 13$ m ($0.325R$), $R2 = 19$ m ($0.475R$), $R3 = 30$ m ($0.75R$), $R4 = 37$ m ($0.925R$)

also carried out for Case A.1 based on the setup given in Section 2.2.1. All the results are compared with field measurement data of the same turbine [31]. Note that it is not possible to have zero turbulence in the field. Therefore, the measurement data was averaged (binned) from azimuth (θ) 0 to 360 degrees.

Figures 8 and 9 present the blade section normal force (perpendicular to local chord orientation) characteristics over the azimuth angle computed using CFD, BEM and Vortexline approaches. Four different radial stations (measured from the center of rotation) are considered at 13 m ($0.325R$), 19 m ($0.475R$),30 m ($0.75R$) and 37 m ($0.925R$). The grey shaded area illustrates the standard deviation of the measured values from the experiment. It can be seen that the BEM results change depending on the employed polar data. The same trend is observed for the Vortexline results. The standard polar data fails to predict the amplitude of the force due to combined wind shear and yaw misalignment effects, especially at $R2$ both for the BEM and Vortexline based calculations. The trend of the computed loads is even incorrect at this radial station when the standard polar data is used. In contrast, the 3D extracted polar data from high fidelity CFD simulation agrees very well with the fully resolved CFD results and field measurement data. The reason for this discrepancy especially at $R2$ can be explained in Figure 10 where the local angle of attack (sampled from Vortexline simulations) and the associated input polar data are presented. It can be seen that the angle of attack at this blade section is within $9° < \alpha < 14°$. The standard polar data shows an indication of stall at this range, which is critical as this affects the characteristics of the simulation results. In contrast, such

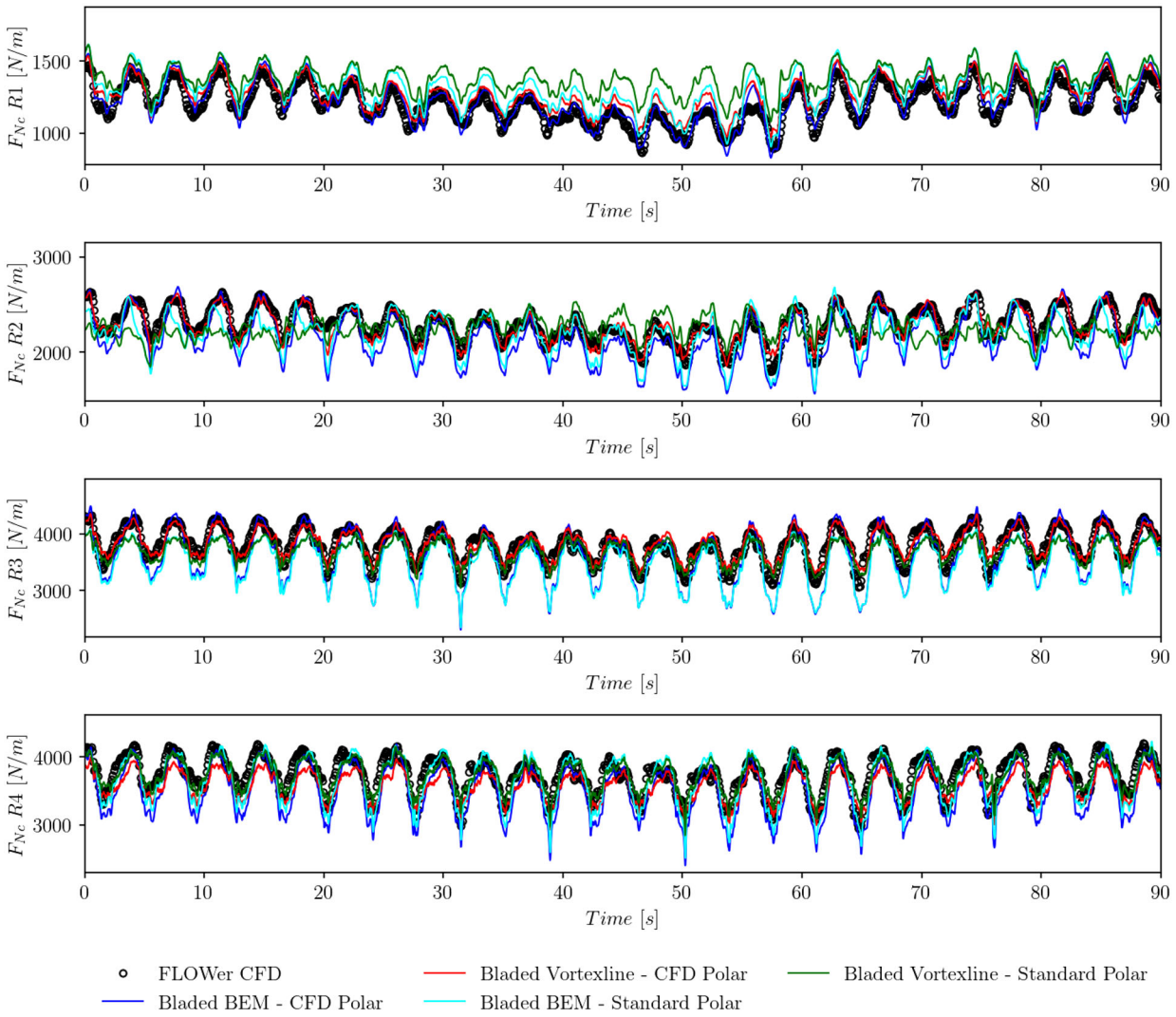

FIGURE 16 Timeseries alignment of the blade section normal force for Case A.2. Four radial stations are reported: $R1 = 13$ m ($0.325R$), $R2 = 19$ m ($0.475R$), $R3 = 30$ m ($0.75R$), $R4 = 37$ m ($0.925R$)

behavior does not appear in the 3D CFD synthesized data as well as the field measurement values.

A similar assessment is made for the blade section chordwise loads in Figure 11 for BEM results and Figure 12 for Vortexline results. All polar datasets seem to be able to reproduce the trend of the chordwise loads fairly well, both for BEM and Vortexline computations. This shows that the discrepancies are mostly originated from the lift forces of the blade sections, while drag is of less concern. Note that the influence of drag is comparable to lift for the blade chordwise force.

The analyses made for the blade section normal and chordwise loads confirm that the selection of the polar data is of highly importance for loads analyses in engineering modeling. The obtained finding indicates the high value of the 3D CFD data for engineering model simulations since the adopted polar data is able to be generalized to different cases - not only bounded to the case where the polar data was extracted from. In fact, the synthesized CFD polar data was obtained from the steady state computations but is still valid for usage under unsteady conditions.

3.1.2 | Impacts of inflow turbulence

The impacts of inflow turbulence on the loads will be discussed in this section. The engineering model calculations were done by adopting the 3D CFD polar data since this is proven to be more accurate as highlighted in Section 3.1.1. A fully resolved CFD simulation was carried out according to the conditions specified in Table 2 for Case A.2 with the numerical setup described in Section 2.2.1. To provide a better overview about the turbulence influence, results from Case A.1 are used for comparison. All the results are compared with field measurement data of the same turbine [31]. The inflow data for engineering model calculations were obtained based on the method described in Section 2.4. Since field measurement data of the inflow at a met-

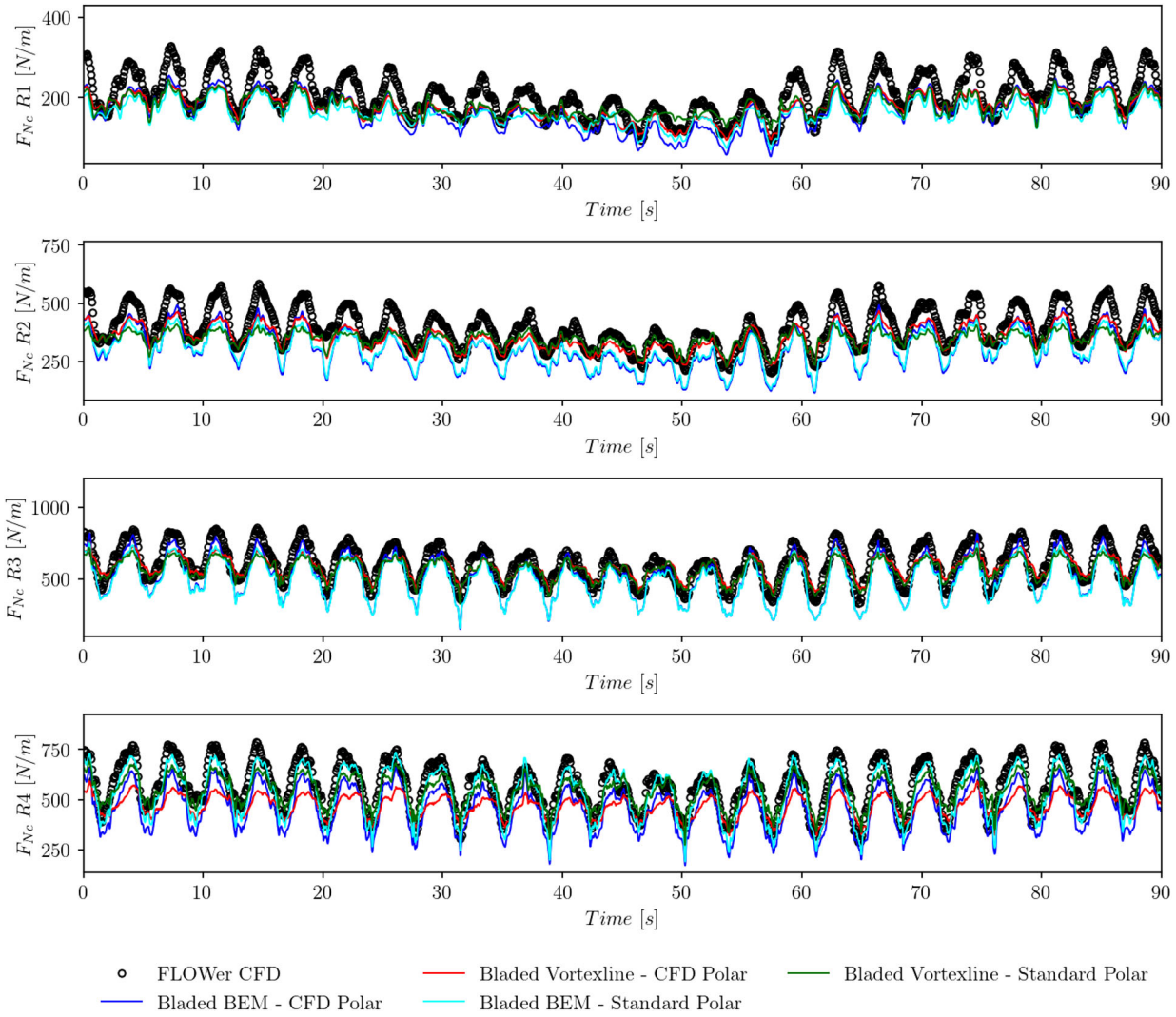

FIGURE 17 Timeseries alignment of the blade section chordwise force for Case A.2. Four radial stations are reported: $R1 = 13$ m ($0.325R$), $R2 = 19$ m ($0.475R$), $R3 = 30$ m ($0.75R$), $R4 = 37$ m ($0.925R$)

mast upstream of the turbine was available, key input parameters such as the turbulence intensity and the shear exponent were adjusted to match with the measurement data. This process was documented in the final report of the IEA Wind Task 29 project in [32].

Figures 13 and 14 depict the results comparison for the chord normal and tangential forces, respectively. It can be seen that the normal loads at $R1$ for cases incorporating inflow turbulence agree fairly well to each other. The non turbulent cases (BEM and Vortexline from Case A.1) show a slightly higher load approaching the top side of the rotor, that is, when the azimuth angle is close to the azimuth angle of 0° or 360°. For the neighboring measured station at $R2$, it can be seen that the similar behavior occurs. Furthermore, now the lowest variation of the normal loads obtained from BEM results (from Case A.2) are also smaller than the Vortexline and CFD results. However, all computed results are still within the range of the measured fluctuations. Note that the measurement was done much longer than the simulations, and such that not all turbulent eddies were simulated. This characteristic is further pronounced at a larger blade station at $R3$. For the most outboard measurement station at $R4$, there is an indication that the normal loads obtained from CFD results are higher than most simulation results. The same characteristics are observed for the tangential loads in Figure 14 for all blade stations. Despite all the described discrepancies, the simulation results are generally in a very good agreement and the trend of the loads is highly comparable.

To better evaluate the source of the discrepancies and to enable future improvement potentials, the dynamics of the axial induction factor (normalized by the the local undisturbed axial velocity) is plotted in Figure 15. For these analyses, only engineering model results are presented since the induced velocity was not available from the CFD and experimental data.

It can be seen in Figure 15 that the axial induction factor (a) varies greatly along the azimuth angle and shows large differences between modeling strategies, especially approaching the

TABLE 3 Test cases considered for the 10 MW wind turbine computations

Case	U_∞ [m/s]	n [rpm]	α_p [deg]	α_s [-]	φ [deg]	TI_X [%]	TI_Y [%]	TI_Z [%]	Models
Case B.1	4	6	0	0	0	0	0	0	CFD/BEM/Vortexline
Case B.2	5	6	0	0	0	0	0	0	CFD/BEM/Vortexline
Case B.3	6	6	0	0	0	0	0	0	CFD/BEM/Vortexline
Case B.4	8	6.8738	0	0	0	0	0	0	CFD/BEM/Vortexline
Case C.1	8	6.8738	0	0	0	23	16.1	12.5	CFD/BEM/Vortexline

blade tip although the computed forces are highly comparable. The axial induction factor for BEM results (both with and without inflow turbulence) increases approaching the lower side of the rotor at 180°. It becomes clear that BEM results incorporating inflow turbulence are characterized with the largest induction variations. This directly influences the angle of attack and ultimately the blade loads. As a consequence, this effect becomes responsible for the lower loads obtained from BEM results with inflow turbulence in Figures 13 and 14.

The same characteristics as for BEM results are observed for the Vortexline results without inflow turbulence in Figure 15, that is, the axial induction factor increases approaching $\theta = 180°$. When turbulence is introduced into the simulations, it can be seen that the induction dynamics changes and this effect is only seen for the Vortexline simulations. This shows that the influence of the inflow turbulence on the wake dynamics is not captured by BEM based results. On a further note, the axial induction factor is relatively high for the chosen test case which also poses a challenge for BEM modeling under turbulent wake state conditions. These observations highlight possible improvements for future engineering model developments. This effect might be related to the dynamic wake assumption of BEM which smears out the local induction dynamics. Future work to improve the sensitivity of BEM to local flow changes can be done by using vortexline data as the reference for tuning or devising a dynamic wake model.

3.1.3 | Timeseries alignment

As the turbulent inflow for Case A.2 was generated using dedicated CFD extraction method with timeshift applied (see Section 2.4), it becomes possible to directly compare the timeseries obtained from engineering model and CFD simulations. The loads acting on chord normal and tangential directions at four radial stations are plotted in Figures 16 and 17, respectively. For comparison, engineering model results obtained from simulations employing the standard polar data are also presented.

The normal loads timeseries in Figure 16 shows that the alignment with the CFD data is slightly affected by the polar data being used. This is actually interesting because the inflow data for all engineering simulations is exactly the same. This occurs in the blade inboard area where the three-dimensional effects are strong. For example, BEM and Vortexline results with the standard polar data overestimate the other models between 20 s and 55 s. The reaction of the local induction due to changes in wind speed seems to be delayed as the rotor loads balance the effects out. As for the cases employed with the 3D CFD polar data, the alignment with the CFD results can be improved. Note again that the 3D CFD polar data was generated under steady inflow conditions which was totally different than the simulated turbulent flow case.

3.2 | 10 MW wind turbine

This section is dedicated for evaluating the simulation results of the 10 MW turbine considered in the studies. Two groups of test cases were evaluated, one under steady state condition and one under turbulent inflow conditions. Details of the steady state test cases (labeled B) and the turbulent test case (labeled C) are given in Table 3. For the turbulent case, a high turbulence intensity was defined to fully explore the influence of turbulence on a large wind turbine rotor. The CFD simulations presented in this section were submitted to the Vortex Loads project [45] as the contribution of the University of Stuttgart. Engineering model simulations were computed by utilizing BEM and Vortexline approaches by adopting standard polar data and the synthesized 3D CFD polar data described in Section 2.3. The standard polar was obtained from two-dimensional CFD simulations of 8 different blade stations constructing the blade from Bangga et al. [16, 17]. These two-dimensional polar data was corrected to account for three-dimensional effects by adopting the correction model according to Chaviaropoulos and Hansen [20].

3.2.1 | Steady state case

The results of the steady state cases for the blade section normal and tangential (perpendicular and parallel to the local chord orientation, respectively) forces are depicted in Figures 18 and 19, respectively. It becomes obvious that the results of engineering model calculations are improved when the 3D CFD polar data was adopted. This occurs especially in the root area where the three-dimensional effects cannot be neglected. These characteristics become more pronounced for large wind turbines because the airfoil thickness is large, which is prone to flow separation.

Bangga et al. [16, 17] demonstrated how the flow field being altered significantly when three-dimensional effects are consid-

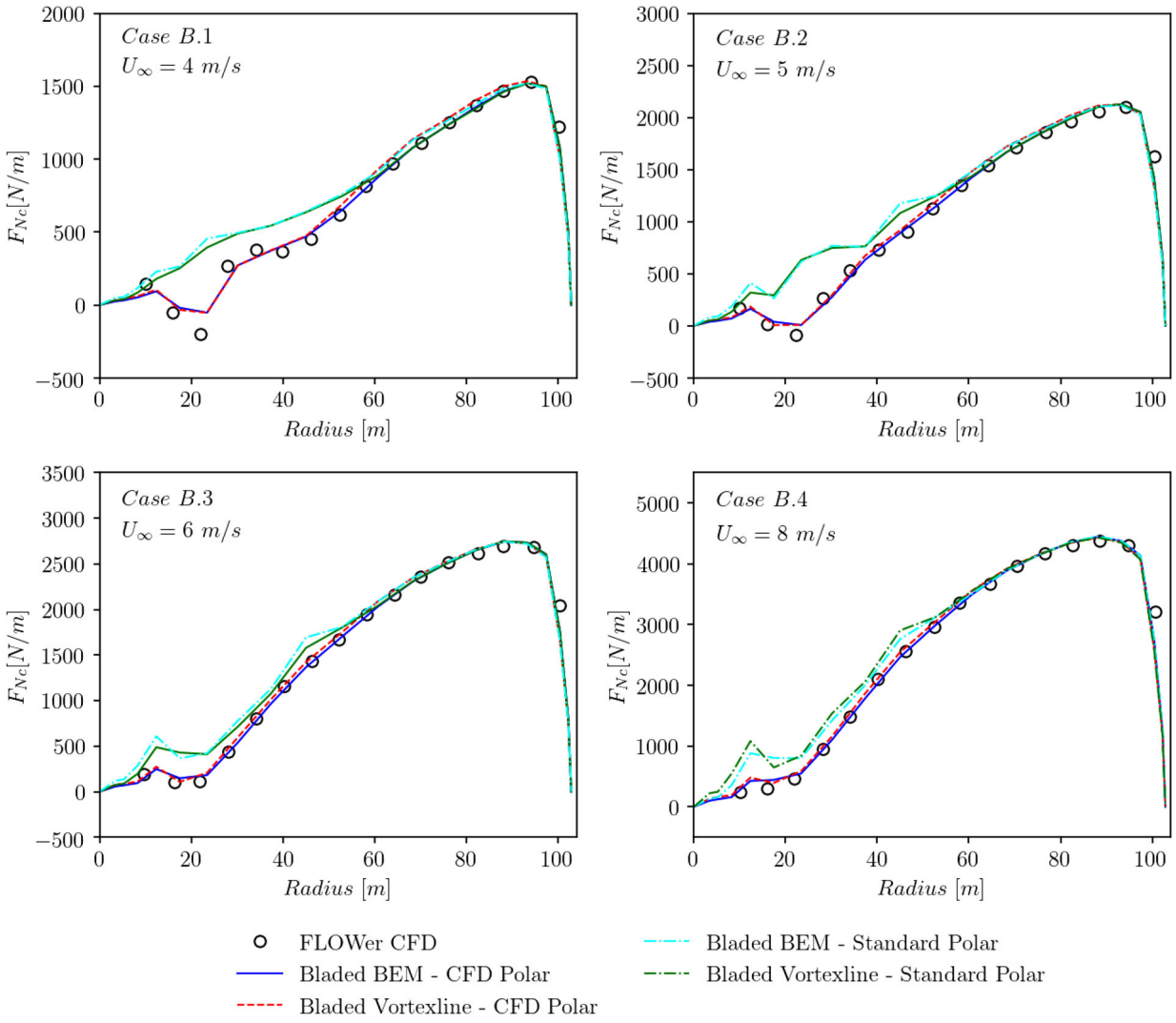

FIGURE 18 Blade section normal force of the 10 MW wind turbine obtained from engineering models and CFD computations for four wind speed cases

ered, as illustrated clearly in Figure 20. The three-dimensional influences in the root area are associated with the Himmelskamp effects due to the centrifugal pumping and the Coriolis acceleration. These induce boundary layer thinning and flow field stabilization and in return yield delayed flow separation compared to the corresponding two-dimensional situation.

The three-dimensional effects in the root area are traditionally corrected using empirical models such as those from Bak et al. [19] or Chaviaropoulos and Hansen [20]. The empirical correction model yields uncertainty which varies from one case to another. As a huge number of load cases need to be performed in designing and assessing wind turbines, there is no silver bullet to definitely declare the correction works for all cases. These empirical models were developed many years back and no extensive calibrations have been made for the current standard of wind turbine size. The proposed three-dimensional CFD polar data can be an alternative to this classical approach. The required computational effort is justified since only steady state CFD simulations will be required for generating the polar data, and this is many orders of magnitude cheaper than transient CFD simulations under realistic inflow conditions.

3.2.2 | Turbulent inflow case

Figures 21 and 22 present the timeseries of the normal and chordwise forces, respectively, at three different radial stations: 50 m (0.485R), 70 m (0.680R) and 95 m (0.923R). Note that the rotor radius reaches 102.9 m for this turbine. Engineering model calculations are compared against CFD simulation results under comparable inflow conditions. The computations were done by adopting the extracted 3D CFD polar data both for BEM and Vortexline methods. The turbulent inflow for engineering model calculations was generated based on the approach described in Section 2.4, making it possible to compare the timeseries alignment.

It can be observed that engineering model results (both BEM and Vortexline) align fairly well with the CFD simulation results.

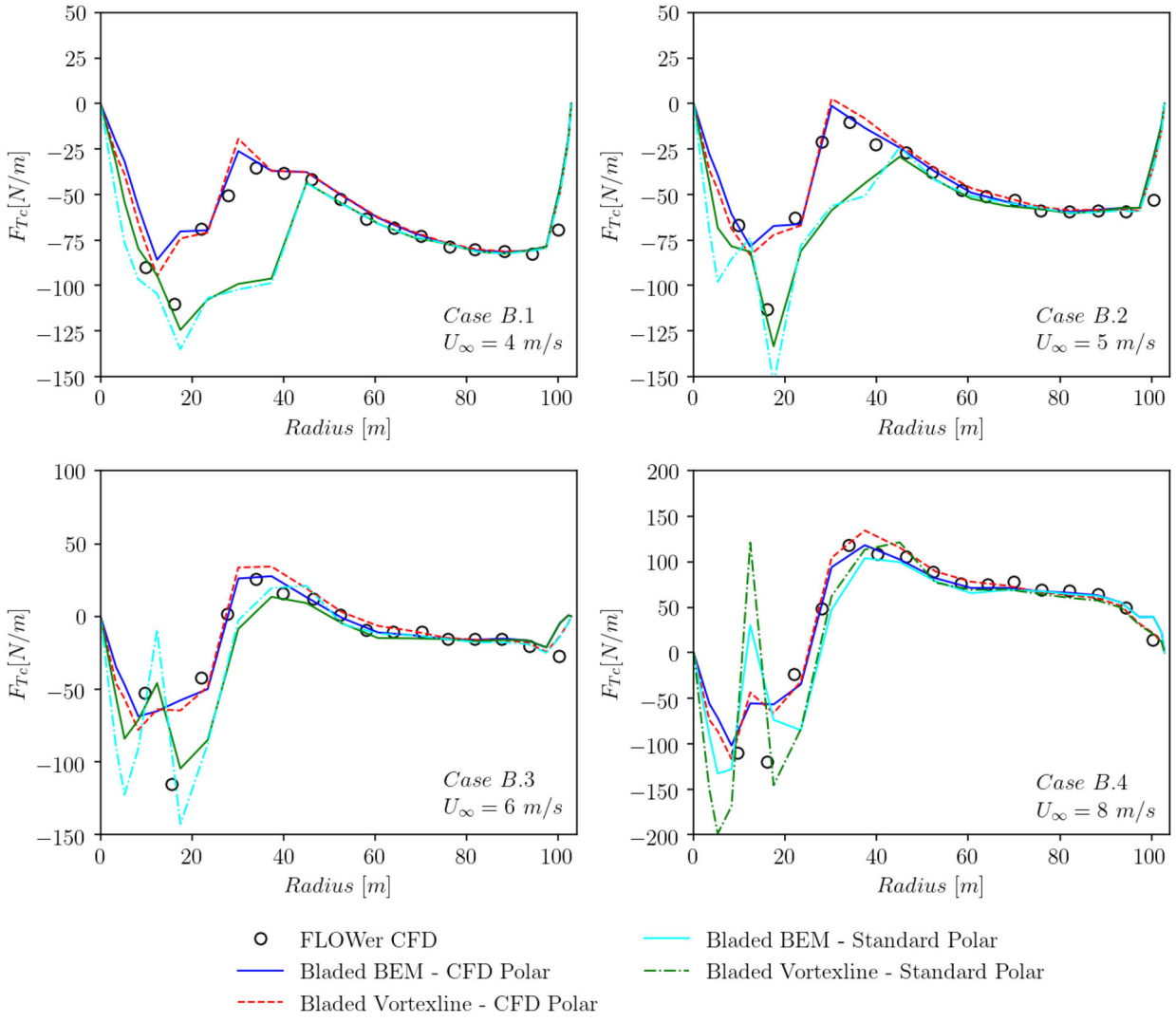

FIGURE 19 Blade section chordwise force of the 10 MW wind turbine obtained from engineering models and CFD computations for four wind speed cases

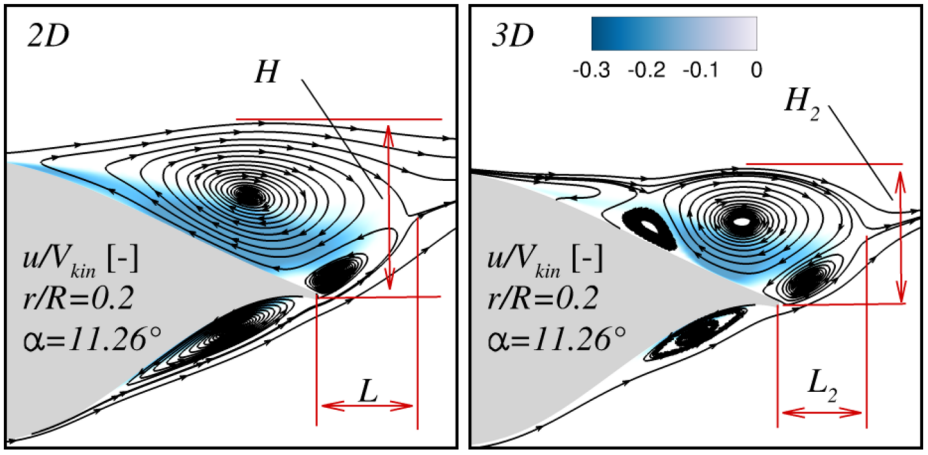

FIGURE 20 Nondimensional velocity (relative to local kinematic velocity) field near the airfoil section of the 10 MW wind turbine rotor. Separation area is significantly reduced for the 3D case, $H_2 < H$ and $L_2 < L$. The area of the negative streamwise velocity (blue color) is remarkably smaller in the 3D case [16, 17]

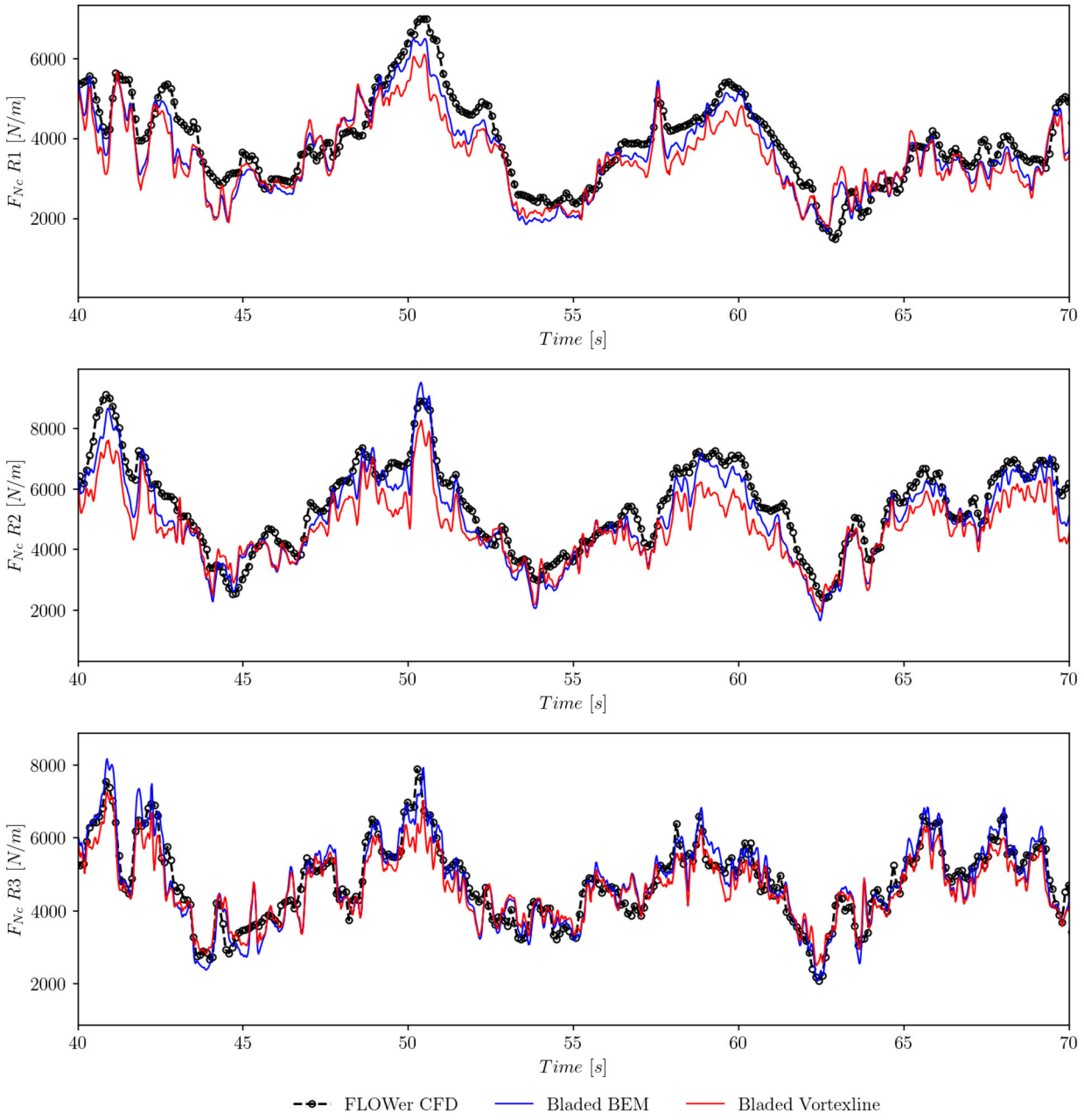

FIGURE 21 Blade section normal force of the 10 MW wind turbine obtained from engineering models and CFD computations under turbulent inflow conditions (Case C.1). Three radial stations are reported: $R1 = 50$ m ($0.485R$), $R2 = 70$ m ($0.680R$), $R3 = 95$ m ($0.923R$)

This signifies the consistency of the adopted approach as the same behavior was observed for the 2.3 MW wind turbine case in Section 3.1. One major finding obtained from observing Figures 21 and 22 is that the Vortexline results underestimate the maximum loads from CFD simulations. In contrast, BEM is able to reconstruct the loads very well despite all the assumptions adopted. Having integrated the loads into the flapwise and edgewise bending moment at the rotor center of rotation, Figure 23 demonstrates that this behavior is also observed for the integrated parameters.

To evaluate this observation in a greater depth, the dynamic characteristics of the axial induction factor (a) and axial induced velocity (u_{ind}) are plotted in Figure 24. The axial undisturbed wind speed (u) at the local blade section is also plotted for comparison. It can be seen that the axial induction factors from both simulations lie around the same mean level, but the fluctuations are inherently different. This is in contrast to the loads observed in Figures 21 and 22. For instance, the axial induction factor decreases at 53 s for Vortexline simulations while it increases for the BEM results. To trace the source of this discrepancy, the induced velocity is also plotted in Figure 24. Now it becomes clear that the induced velocity decreases for the Vortexline results but it remains almost stationary for the BEM results. The trend of the axial induc-

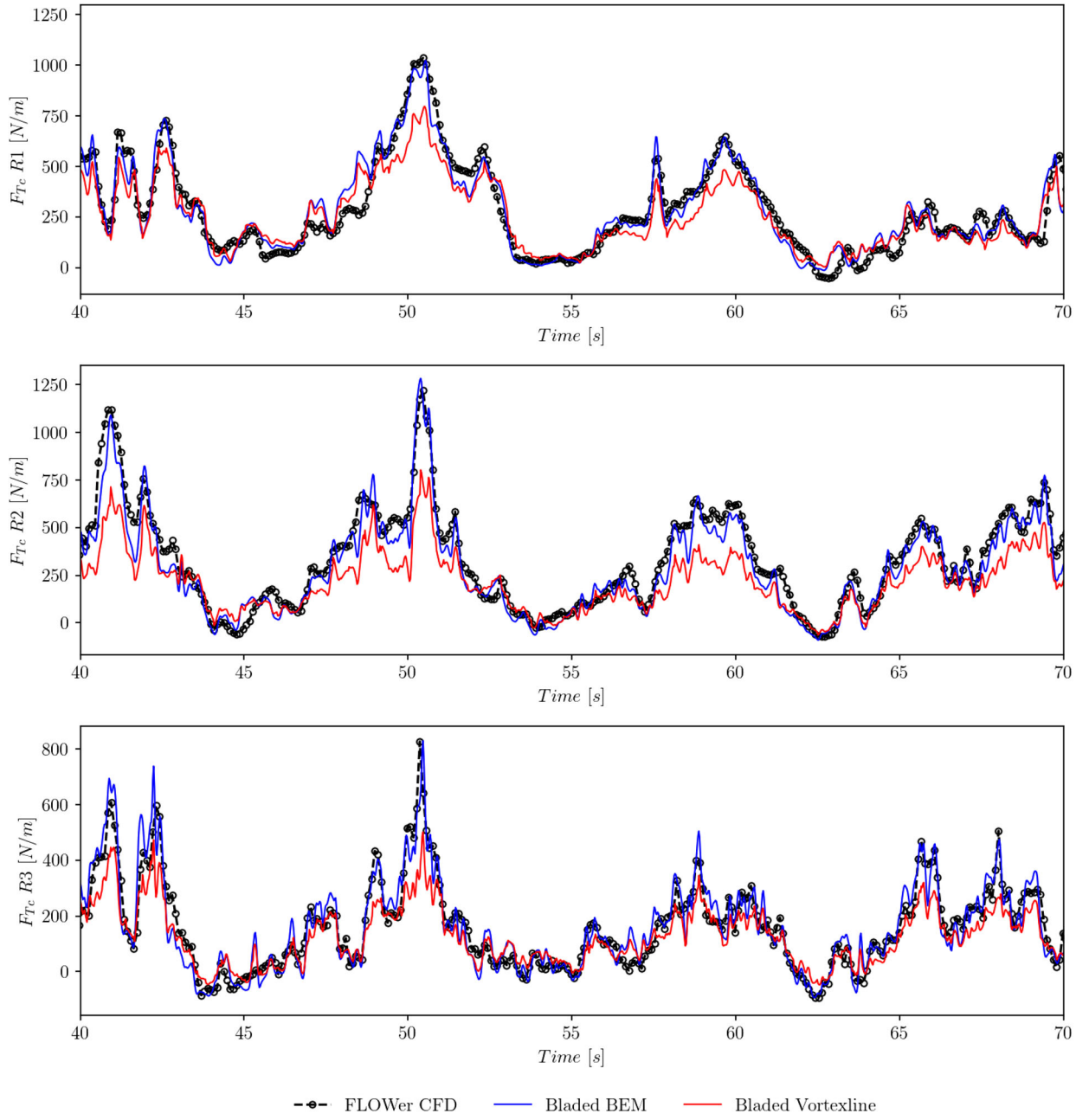

FIGURE 22 Blade section chordwise force of the 10 MW wind turbine obtained from engineering models and CFD computations under turbulent inflow conditions (Case C.1). Three radial stations are reported: $R1 = 50$ m ($0.485R$), $R2 = 70$ m ($0.680R$), $R3 = 95$ m ($0.923R$)

tion for Vortexline results is inline with the local axial wind speed at the corresponding blade section. This variation is plausibly more physical than the stationary induction trend obtained from BEM. In accordance with the conclusion obtained from the 2.3 MW wind turbine case, Vortexline seems to be more sensitive to changes in inflow variation which affects the wake dynamics. Such characteristics are not captured in BEM based calculations and can be a subject of future engineering model developments.

3.3 | Discussion on the rotor size influence

The analyses performed for the 2.3 MW wind turbine in Section 3.1 and for the 10 MW wind turbine in Section 3.2 highlight the influence of the rotor size on engineering calculation results. From the studies, it can be seen that the overall agreement between engineering models and experimental data as well as CFD results becomes better when the sectional aerodynamic data is replaced with the synthesized 3D CFD polar. The

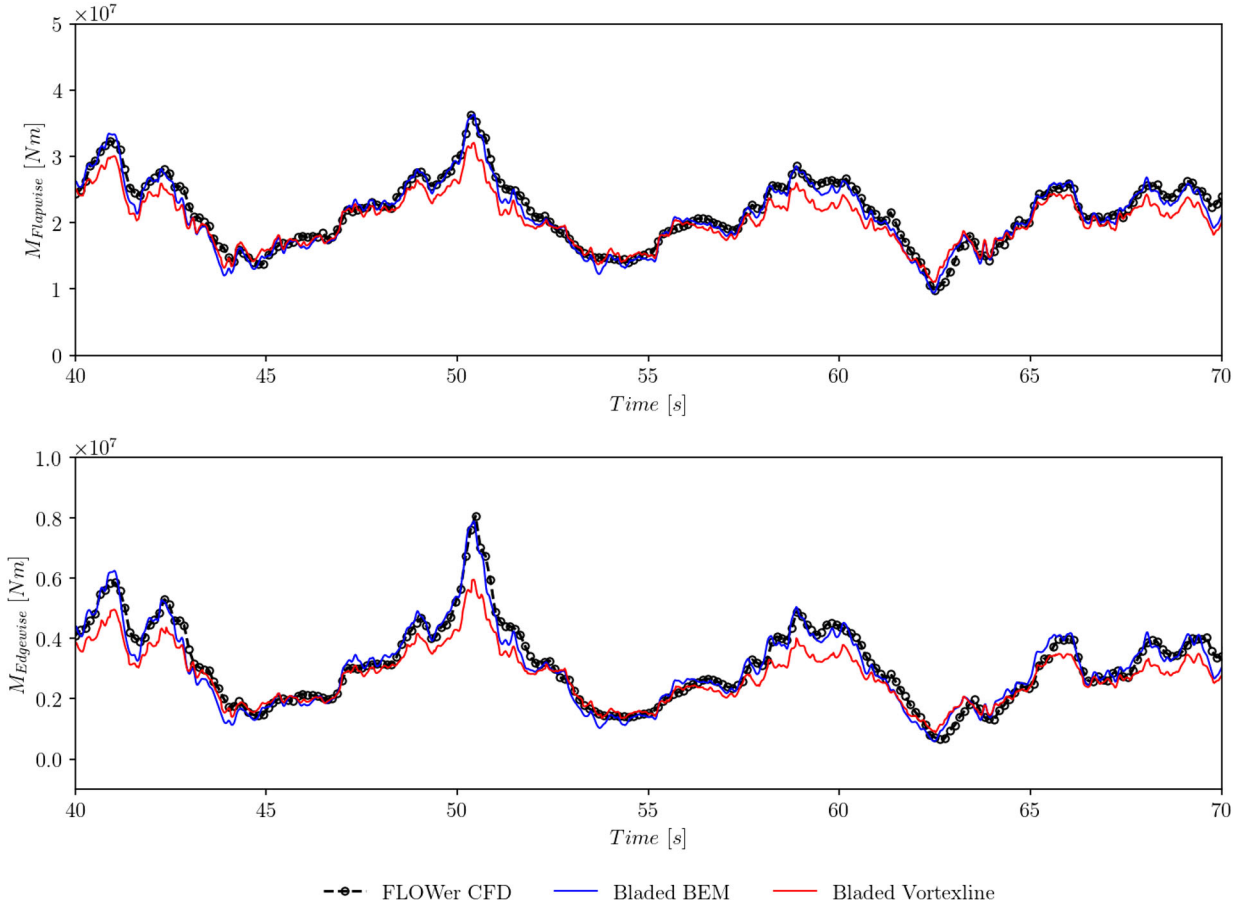

FIGURE 23 Rotor center flapwise (top) and edgewise (bottom) bending moments obtained from blade-1 obtained from engineering model and CFD computations of the 10 MW wind turbine

approach is confirmed for two turbines having completely different rotor sizes ($R = 40$ m against $R = 102.9$ m). This clearly suggests that the usage of the 3D CFD polar data is applicable for the load analyses regardless of the wind turbine size. This way, all important physical parameters such as the Reynolds number, Mach number and actual blade section geometry are inherently included in the engineering calculations.

The same key results also apply for the extracted inflow data from the 3D CFD simulations. This approach is successful in aligning the timeseries data between engineering models and CFD results. The method is applicable for wind turbine load analyses regardless of the rotor size. It is important to note again that this approach requires relatively large computational effort. This shall be aimed only when the exact course of the timeseries is of interest, for example to develop advanced control techniques in complex situations.

The third key point about the rotor size influence lies on the result differences between BEM and vortexline methods. It is clear from Section 3.1 (2.3 MW turbine) that Vortexline has a better agreement with experiment and CFD than BEM results. In contrary, BEM agrees with CFD data better than Vortexline for the 10 MW turbine in Section 3.2.

The induction dynamics in Figures 15 and 24 hold the answer to this inconsistency. The 10 MW rotor ($a \approx 0.2$) operates at a much lower induction level than the 2.3 MW rotor ($a \approx 0.4$). This means that the lower rotor is challenged by the turbulent wake state effect. BEM relies on the usage of the empirical model for modeling this aspect (in this case the Glauert correction was applied), and this can lead to inaccuracy. On the other hand, the induction dynamics in Vortexline are directly influenced by the wake solutions, allowing a more accurate solution.

When the 10 MW rotor is calculated, the low induction characteristic of the rotor causes the full development of the wake takes longer. This means the induction at the blade sections are influenced by the strength of the wake vortices up to long wake distance. As a consequence, more wake points shall be included in Vortexline computations to consider these effects. The accuracy of the Vortexline calculations in Section 3.2 may be improved by increasing the number of wake points. Despite that, this increases the computational time significantly from a couple of minutes to days, preventing practical engineering applications for load analyses. Since the real load analyses according to IEC may have more than 1000 load cases in reality, the computational effort in Vortexline shall be reduced

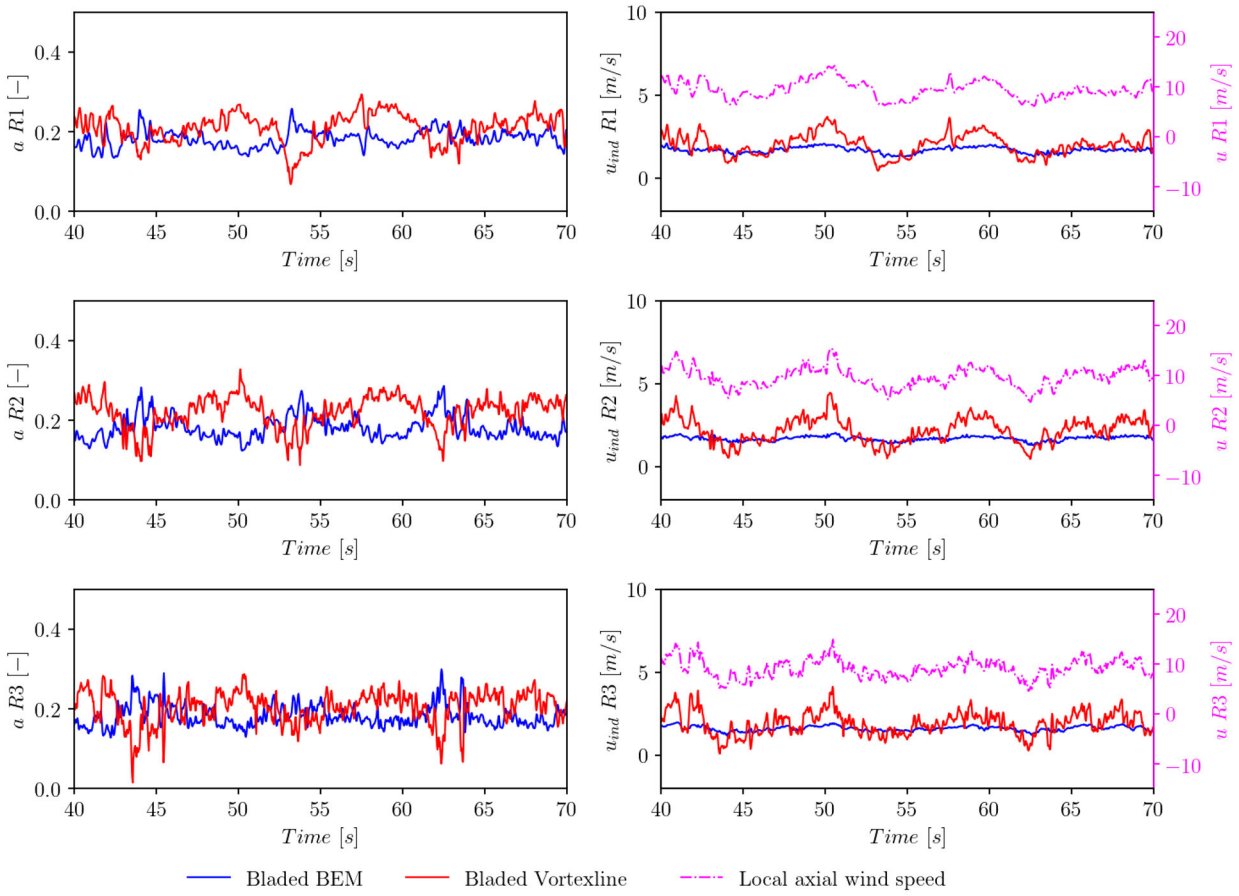

FIGURE 24 Induction dynamics comparison between BEM and Vortexline results for Case C.1. Three radial stations are reported: $R1 = 50$ m (0.485R), $R2 = 70$ m (0.680R), $R3 = 95$ m (0.923R)

TABLE 4 Flow conditions and turbine setup for simulating the 10 MW wind turbine under an IEC design load case

Case	U_∞ [m/s]	n [rpm]	α_p [deg]	α_s [-]	φ [deg]	TI_X [%]	TI_Y [%]	TI_Z [%]	Models
Case D.1	25	0.0	75	0.11	−8.0	11	7.7	5.5	BEM/Vortexline

as low as possible. Future work may be aimed at improving the accuracy of Vortexline computations without having to include lots of wake points, for example, by applying some empirical corrections.

3.4 | IEC design load case

The last test case investigated in this paper adopts an IEC design load case (DLC) according to the IEC standard - Edition 4 [60]. For this study, the 10 MW wind turbine was adopted. The chosen load case is DLC 6.1 that simulates wind turbine loads in parked conditions. This flow situation yields relatively high angles of attack over the whole blade stations. The turbine was exposed to an extreme wind speed model (EWM) with a return period of 1 year. The model was applied to a reference velocity (wind speed) of 25 m/s and a shear exponent of 0.11. Details of the flow conditions are given in Table 4.

The resulting rotor loads are plotted in Figure 25 for different simulation models and polar data sources. The simulations were carried out for 450 s, but only the a sample of 200 s is presented for clarity of the observation. It can be seen that the resultant moment at the rotor center varies depending on the polar data, where the simulations adopting the 3D CFD polar predict a higher resultant moment. The usage of the 3D CFD polar data reduces slightly the rotor torque. A clear discrepancy between the two polar data is observed for the rotor thrust. It is observed that thrust level is overestimated when the standard polar data is used. This is in agreement with the observation made in Section 3.2 for the blade normal forces. A deeper observation is made by evaluating the dynamic polar data from four blade stations in Figure 26. The dynamic stall effects are clearly

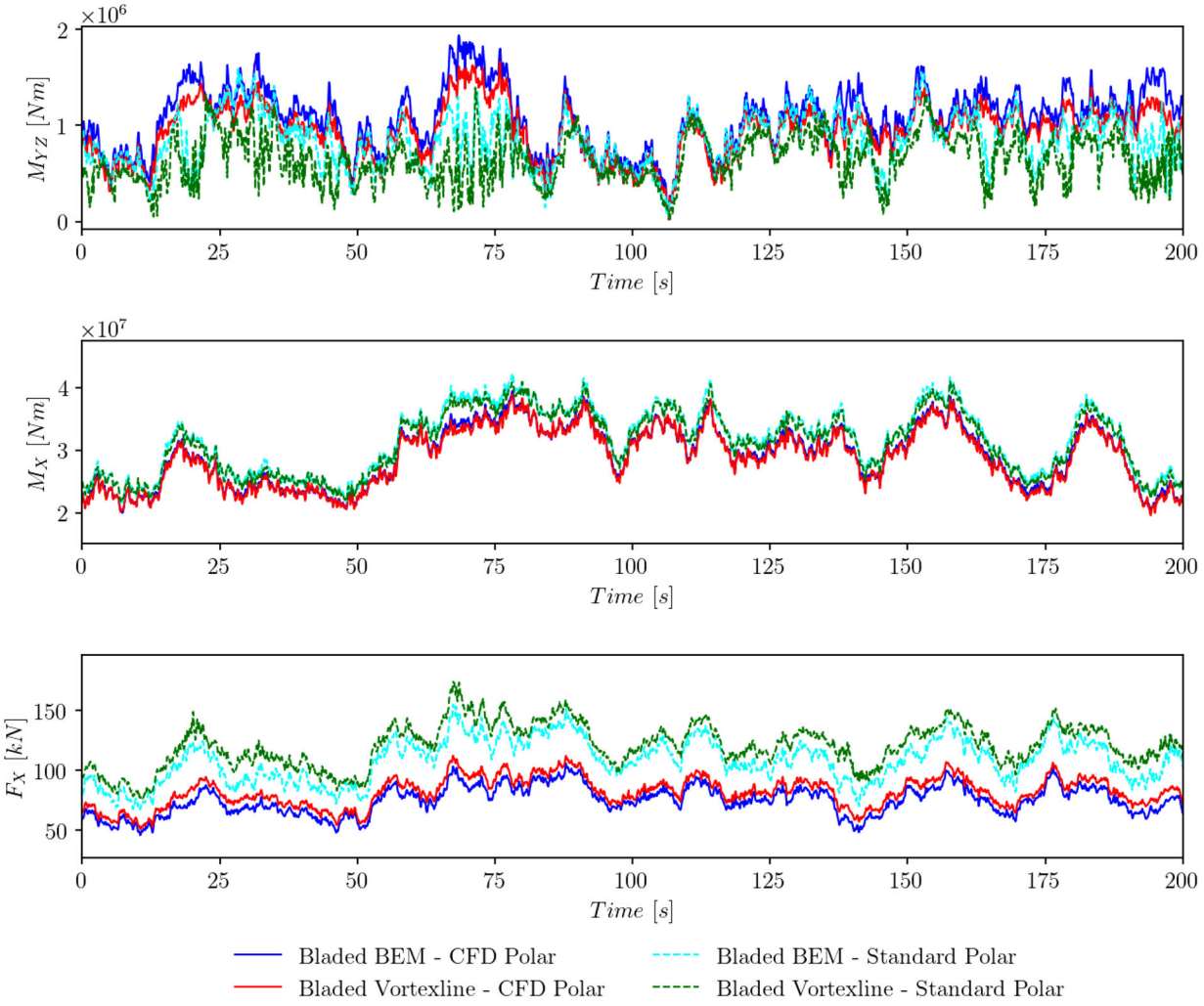

FIGURE 25 Rotor loads recorded at the center of rotation for the resultant moment (M_{YZ}), torque (M_X) and thrust (F_X)

seen for these four radial stations as the local angles of attack are relatively large. The agreement between different polar datasets becomes poorer approaching the blade root where the three-dimensional effects are large. The deviation also increases once the blade stations approach stall. This further highlights the importance of careful consideration in selecting the polar data used for load analyses of wind turbines.

To further summarize different methods evaluated in this paper, Table 5 provides an illustration of the key strengths and challenges associated with each method. This involves the usage of different polar and inflow data as well as adopting BEM or Vortexline method.

4 | CONCLUSIONS AND REMARKS

The present studies provide comprehensive evaluations of the load analyses of wind turbines with different rotor sizes. CFD and engineering model computations were adopted to calculate the loads acting on the turbines at various flow conditions. The usage of synthesized 3D CFD polar data was demonstrated for various cases and discussions into the physics were provided. The following conclusions might be drawn from the paper:

- 3D CFD polar data can be generated by utilizing steady inflow conditions but is able to generalize to various challenging cases including strong shear, yaw misalignment, high turbulence and parked conditions.
- The usage of the 3D polar data is verified for medium and large wind turbine sizes.
- The results of the engineering model simulations are in a good agreement with CFD and experimental data.
- Timeseries alignment with CFD results is made possible if a dedicated consistent inflow condition is imposed.
- The agreement between the standard polar data with the 3D CFD polar data deteriorates approaching the blade root and when the blade sections are approaching stall conditions.
- Three-dimensional effects in the root area remain strong for large wind turbine and empirical correction models are not sufficient for challenging flow conditions.

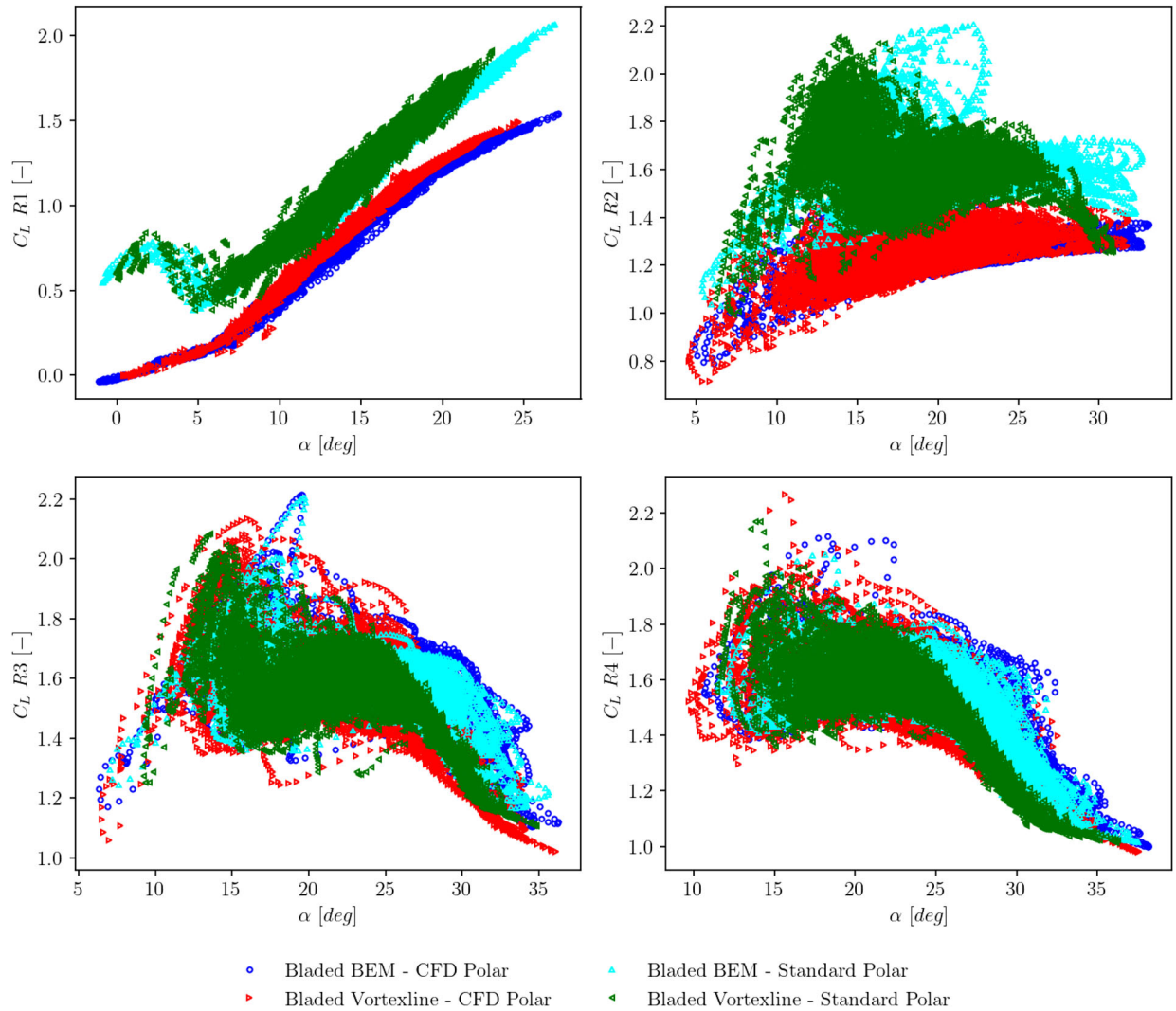

FIGURE 26 Dynamics of the lift coefficient of the 10 MW wind turbine for Case D.1. Four radial stations are reported: $R1 = 25$ m ($0.194R$), $R2 = 45$ m ($0.437R$), $R3 = 70$ m ($0.680R$), $R4 = 95$ m ($0.923R$)

TABLE 5 Characteristics of the simulation strategy using engineering models

Model	Strength	Challenge
Vortexline	Relatively accurate	High computational effort
	Induction is sensitive to local flow	Accuracy and speed depend on wake points
	Appropriate for high induction case	Still based on inviscid method
	Useful for wake study	
BEM	Accuracy is acceptable for most cases	Induction is less sensitive to local flow
	Industrially matured	Huge number of model/assumption variations
	Numerically stable and robust	Lower accuracy for high induction case
3D CFD polar data	Accurate for most flow conditions	Preparatory computational effort is required
	Can be generated for many blade sections	Require angle of attack extraction
CFD inflow data	Suitable for timeseries alignment	Huge preparatory computational effort is required

- The induced velocity obtained from BEM computations is less sensitive to changes of the inflow conditions, in contrast to the Vortexline results. This highlights a possible improvement area in future engineering model developments.
- Future studies might be aimed at improving the accuracy of Vortexline calculations for turbines having low induction levels without considering a huge number of wake points.

Based on the studies, it becomes clear that the usage of the 3D CFD polar data is recommended for improving the accuracy of engineering model calculations, which in turn directly contributes to the increased reliability of the wind turbine loads analyses. The synthesized polar data is not only useful for modeling the Himmelskamp effect, but this also includes the effect of other important physical parameters such as the Reynolds number, Mach number (especially for large blade near the tip area), radial variation of the pressure field, blade geometry effect etc. These parameters affect the flow field surrounding the rotor and ultimately the rotor loads. Furthermore, extracting the inflow data from CFD simulations is also suggested for comparing the timeseries alignment with CFD simulations. However, this requires a greater effort and computational expenses but has little influence on the overall statistics. Therefore, this approach shall be used only when timeseries assessment is of interest, e,g. for designing advanced control strategies.

AUTHOR CONTRIBUTIONS

Galih Bangga: Conceptualization, data curation, formal analysis, investigation, methodology, resources, validation, writing - original draft, writing - review and editing. Steven Parkinson: Writing - review and editing. Thorsten Lutz: Writing - review and editing.

ACKNOWLEDGEMENTS

The authors gratefully acknowledge the following institutions: the High Performance Computing Center Stuttgart (HLRS) for the computational resources in performing the CFD simulations, the IEA Wind Task 29 consortium (as well as Task 47) for providing the geometry of the 2.3 MW NM-80 wind turbine and the AVATAR consortium & the Vortex Loads project for providing the geometry of the 10 MW AVATAR wind turbine.

CONFLICT OF INTEREST

The authors have declared no conflict of interest.

DATA AVAILABILITY STATEMENT

Data can be made available by contacting the corresponding author

ORCID

Galih Bangga https://orcid.org/0000-0001-8052-0441

REFERENCES

1. Bangga, G., Lutz, T.: Aerodynamic modeling of wind turbine loads exposed to turbulent inflow and validation with experimental data. Energy 223, 120076 (2021)
2. Betz, A.: Das Maximum der theoretisch möglichen Ausnutzung des Windes durch Windmotoren. Zeitschrift fur das gesamte Turbinenwesten 20, (1920)
3. Glauert, H.: The Elements of Aerofoil and Airscrew Theory. Cambridge University Press, Cambridge (1983)
4. Glauert, H.: Airplane propellers, aerodynamic theory. (durand series, volume iv, division l), (1963)
5. Glauert, H., et al.: A General Theory of the Autogyro, vol. 1111. HM Stationery Office, London (1926)
6. Micallef, D., Sant, T., Aissaoui, A., Tahour, A.: A review of wind turbine yaw aerodynamics. In: Wind Turbines-Design, Control and Applications. IntechOpen, London (2016)
7. Coleman, R.P., Feingold, A.M., Stempin, C.W.: Evaluation of the induced-velocity field of an idealized helicoptor rotor. Technical report, NASA, Washington DC (1945)
8. Pitt, D.M., Peters, D.A.: Theoretical prediction of dynamic-inflow derivatives. In: 6th European Rotorcraft & Powered Lift Aircraft Forum, 1980, Part 2. University of Bristol (1980)
9. White, F., Blake, B.B.: Improved method predicting helicopter control response and gust sensitivity. American Helicopter Society, Alexandria, VA (1979)
10. Schepers, J.G.: Engineering models in wind energy aerodynamics: Development, implementation and analysis using dedicated aerodynamic measurements (2012)
11. Rahimi, H., Hartvelt, M., Peinke, J., Schepers, J.: Investigation of the current yaw engineering models for simulation of wind turbines in BEM and comparison with CFD and experiment. J. Phys. Conf. Ser 753, 022016 (2016)
12. Madsen, H.A., Riziotis, V., Zahle, F., Hansen, M.O.L., Snel, H., Grasso, F., Larsen, T.J., Politis, E., Rasmussen, F.: Blade element momentum modeling of inflow with shear in comparison with advanced model results. Wind Energy 15(1), 63–81 (2012)
13. Prandtl, L., Betz, A.: Vier Abhandlungen zur Hydrodynamik und Aerodynamik, Vol. 3. Universitätsverlag Göttingen (2010)
14. Shen, W.Z., Mikkelsen, R., Sørensen, J.N., Bak, C.: Tip loss corrections for wind turbine computations. Wind Energy 8(4), 457–475 (2005)
15. Himmelskamp, H.: Profile Investigations on a Rotating Airscrew. Ministry of Aircraft Production (1947)
16. Bangga, G.: Three-dimensional flow in the root region of wind turbine rotors. Kassel University Press GmbH, Kassel (2018)
17. Bangga, G., Lutz, T., Jost, E., Krämer, E.: CFD studies on rotational augmentation at the inboard sections of a 10 MW wind turbine rotor. J. Renew. Sustain. Energy 9(2), 023304 (2017)
18. Lindenburg, C.: Modelling of rotational augmentation based on engineering considerations and measurements (2004)
19. Bak, C., Johansen, J., Andersen, P.B.: Three-dimensional corrections of airfoil characteristics based on pressure distributions. Proceedings of the European Wind Energy Conference, pp. 1–10. European Wind Energy Association, Brussels, Belgium (2006)
20. Chaviaropoulos, P., Hansen, M.O.: Investigating three-dimensional and rotational effects on wind turbine blades by means of a quasi-3D Navier-Stokes solver. J. Fluids Eng. 122(2), 330–336 (2000)
21. Du, Z., Selig, M.: A 3-D stall-delay model for horizontal axis wind turbine performance prediction. 1998 ASME Wind Energy Symposium, p. 21. American Society of Mechanical Engineers, American Institute of Aeronautics and Austronautics, New York (1998)
22. Sørensen, N.N., Michelsen, J., Schreck, S.: Navier–Stokes predictions of the NREL phase VI rotor in the NASA Ames 80 ft× 120 ft wind tunnel. Wind Energy 5(2-3), 151–169 (2002)
23. Pape, A.L., Lecanu, J.: 3D Navier–Stokes computations of a stall-regulated wind turbine. Wind Energy 7(4), 309–324 (2004)
24. Tachos, N., Filios, A., Margaris, D.: A comparative numerical study of four turbulence models for the prediction of horizontal axis wind turbine flow. Proc. Inst. Mech. Eng. Part C: J. Mech. Eng. Sci. 224(9), 1973–1979 (2010)
25. Nigam, P., Tenguria, N., Pradhan, M.: Analysis of horizontal axis wind turbine blade using CFD. Int. J. Eng. Sci. Technol. 9(2), 46–60 (2017)

26. Thé, J., Yu, H.: A critical review on the simulations of wind turbine aerodynamics focusing on hybrid RANS-LES methods. Energy 138, 257–289 (2017)
27. Bangga, G., Lutz, T., Krämer, E.: Root flow characteristics and 3D effects of an isolated wind turbine rotor. J. Mech. Sci. Technol. 31(8), 3839–3844 (2017)
28. Bangga, G.: Comparison of Blade Element Method and CFD simulations of a 10 MW wind turbine. Fluids 3(4), 73 (2018)
29. Schneider, M.S., Nitzsche, J., Hennings, H.: Accurate load prediction by BEM with airfoil data from 3D RANS simulations. J. Phys.: Conf. Series 753, 082016 (2016)
30. Guma, G., Bangga, G., Jost, E., Lutz, T., Krämer, E.: Consistent 3D CFD and BEM simulations of a research turbine considering rotational augmentation. J. Phys.: Conf. Series 1037, 022024 (2018)
31. Aagaard Madsen, H., Bak, C., Schmidt Paulsen, U., Gaunaa, M., Fuglsang, P., Romblad, J., Olesen, N., Enevoldsen, P., Laursen, J., Jensen, L.: The DAN-AERO MW experiments: final report. Danmarks Tekniske Universitet, Risø Nationallaboratoriet for Bæredygtig Energi (2010). orbit. dtu. dk. Accessed 13 November 2017
32. Schepers, J., Boorsma, K., A Madsen, H., Pirrung, G., Bangga, G., Guma, G., Lutz, T., Potentier, T., Braud, C., Guilmineau, E., et al.: IEA Wind TCP Task 29, Phase IV: Detailed Aerodynamics of Wind Turbines (2021)
33. Lekou, D., Chortis, D., Chaviaropoulos, P., Munduate, X., Irisarri, A., Madsen, H., Yde, K., Thomsen, K., Stettner, M., Reijerkerk, M., et al.: Avatar deliverable d1. 2 reference blade design. Technical Report (2015)
34. Bak, C., Zahle, F., Bitsche, R., Kim, T., Yde, A., Henriksen, L., Andersen, P.B., Natarajan, A., Hansen, M.H.: Design and performance of a 10 MW wind turbine. Wind Energy 124 (2013)
35. Kroll, N., Rossow, C.C., Becker, K., Thiele, F.: The MEGAFLOW project. Aerosp. Sci. Technol. 4, 223–237 (2000)
36. Jost, E., Fischer, A., Bangga, G., Lutz, T., Krämer, E.: An investigation of unsteady 3-D effects on trailing edge flaps. Wind Energy Sci. 2(1), 241–256 (2017)
37. Bangga, G., Hutani, S., Heramarwan, H.: The effects of airfoil thickness on dynamic stall characteristics of high-solidity vertical axis wind turbines. Adv. Theor. Simul. 4(6), 2000204 (2021)
38. Kankatala, P., Bangga, G.: Active separation control on thick wind turbine airfoils by means of steady and unsteady blowing. Adv. Theor. Simul. 2(7), 1900077 (2019)
39. Bangga, G., Seel, F., Lutz, T., Kühn, T.: Aerodynamic and acoustic simulations of thick flatback airfoils employing high order DES methods. Adv. Theor. Simul. 5(8), 2200129 (2022)
40. Menter, F.R.: Two-equation eddy-viscosity turbulence models for engineering applications. AIAA J. 32(8), 1598–1605 (1994)
41. Jameson, A., Schmidt, W., Turkel, E.: Numerical solution of the Euler equations by finite volume methods using Runge Kutta time stepping schemes. In: 14th Fluid and Plasma Dynamics Conference. American Institute of Aeronautics and Astronautics, New York (1981)
42. Jiang, G.S., Shu, C.W.: Efficient implementation of weighted ENO schemes. J. Comput. Phys. 126, 202–228 (1996)
43. Robertson, A.N., Wendt, F., Jonkman, J.M., Popko, W., Dagher, H., Gueydon, S., Qvist, J., Vittori, F., Azcona, J., Uzunoglu, E., et al.: OC5 project phase II: validation of global loads of the DeepCwind floating semisubmersible wind turbine. Energy Procedia 137, 38–57 (2017)
44. Vita, L., Ramachandran, G., Krieger, A., Kvittem, M.I., Merino, D., Cross-Whiter, J., Ackers, B.B.: Comparison of numerical models and verification against experimental data, using Pelastar TLP concept. In: International Conference on Offshore Mechanics and Arctic Engineering, vol. 56574, p. V009T09A047. American Society of Mechanical Engineers, New York (2015)
45. Boorsma, K., Wenz, F., Aman, M., Lindenburg, C., Kloosterman, M., WoZ, S.T.: TKI WOZ VortexLoads final report. Technical report, TNO (2019)
46. Boorsma, K., Wenz, F., Lindenburg, K., Aman, M., Kloosterman, M.: Validation and accommodation of vortex wake codes for wind turbine design load calculations. Wind Energy Sci. 5(2), 699–719 (2020)
47. Collier, W., Sanz, J.M.: Comparison of linear and non-linear blade model predictions in Bladed to measurement data from GE 6MW wind turbine. J. Phys.: Conf. Series, vol. 753, p. 082004. IOP Publishing, Bristol (2016)
48. Hach, O., Verdonck, H., Polman, J., Balzani, C., Müller, S., Rieke, J., Hennings, H.: Wind turbine stability: Comparison of state-of-the-art aeroelastic simulation tools. J. Phys.: Conf. Series, vol. 1618, p. 052048. IOP Publishing, Bristol (2020)
49. Verdonck, H., Hach, O., Polman, J., Balzani, C., Braun, O., Müller, S., Rieke, J.: Code-to-code comparison of realistic wind turbine instability phenomena (2021)
50. Boorsma, K., Schepers, G., Aagard Madsen, H., Pirrung, G., Sørensen, N., Bangga, G., Imiela, M., Grinderslev, C., Meyer Forsting, A., Zhong Shen, W., et al.: Progress in validation of rotor aerodynamic codes using field data. Wind Energy Science Discussions, pp. 1–31. Copernicus Publications, Gottingen (2022)
51. Chung, J., Hulbert, G.M.: A time integration algorithm for structural dynamics with improved numerical dissipation: The generalized-α method. J. Appl. Mech. 60(2), 371–375 (1993)
52. Leishman, J.: State-space model for unsteady airfoil behavior and dynamic stall. In: 30th Structures, Structural Dynamics and Materials Conference, p. 1319. American Institute of Aeronautics and Astronautics, Reston, VA (1989)
53. Hansen, M.H., Gaunaa, M., Madsen, H.A.: A Beddoes-Leishman type dynamic stall model in state-space and indicial formulations. (2004)
54. Kloosterman, M.: Development of the near wake behind a horizontal axis wind turbine-including the development of a free wake lifting line code (2009)
55. Harrison, M., Kloosterman, M., Urbano, R.B.: Aerodynamic modelling of wind turbine blade loads during extreme deflection events. J. Phys.: Conf. Series 1037, 062022 (2018)
56. Micallef, D., Kloosterman, M., Ferreira, C., Sant, T., van Bussel, G.: Validating BEM, direct and inverse free wake models with the MEXICO experiment. In: 48th AIAA Aerospace Sciences Meeting Including the New Horizons Forum and Aerospace Exposition, p. 462. American Institute of Aeronautics and Astronautics, Reston, VA (2010)
57. Hansen, M.O., Sørensen, N.N., Michelsen, J.: Extraction of lift, drag and angle of attack from computed 3-D viscous flow around a rotating blade. In: 1997 European Wind Energy Conference. European Wind Energy Association, Brussels, Belgium (1997)
58. Troldborg, N., Sørensen, J.N., Mikkelsen, R., Sørensen, N.N.: A simple atmospheric boundary layer model applied to large eddy simulations of wind turbine wakes. Wind Energy 17, 657–669 (2014)
59. Wenz, F., Boorsma, K., Lutz, T., Krämer, E.: Cross-correlation-based approach to align turbulent inflow between CFD and lower-fidelity-codes in wind turbine simulations. J. Phys.: Conf. Series 1618, 062005 (2020)
60. IEC: Wind energy generation systems-Part 1: Design requirements Ed. 4. International Electrotechnical Commission, Geneva, Switzerland (2019)

How to cite this article: Bangga, G., Parkinson, S., Lutz, T.: Utilizing high fidelity data into engineering model calculations for accurate wind turbine performance and load assessments under design load cases. IET Renew. Power Gener. 17, 2909–2933 (2023). https://doi.org/10.1049/rpg2.12649